POLITECNICO DI TORINO

MASTER's Degree in BIOMEDICAL ENGINEERING

MASTER's Degree Thesis

Design of an indirect bio-impedance measurement system for plant health monitoring

Supervisors

Prof. Danilo DEMARCHI

Ph.D. Umberto GARLANDO

M.Sc. Stefano CALVO

Candidate

MARTA CHIARILLO

December 2022

Abstract

Climate change is the greatest threat of the twenty-first century, endangering the well-being of present and future generations. As a result, climate-smart methods known as smart agriculture have been adopted in recent years.
Proximity plant monitoring is one of several newly developed techniques for more sustainable agriculture. Standard crop and single-plant health tracking methods use sensors to measure environmental parameters such as moisture, lighting, and soil characteristics. This thesis proposes an alternative and novel approach to understanding plant health conditions by directly exploiting a signal that has been injected into the plant's stem. It involves a low-cost device that measures the attenuation state of a signal injected within the plant to measure the stem's impedance, which is known from the literature to be related to water conditions. Since the final device requires energy autonomy, it is battery-powered and consists of transmitting and receiving systems designed to be completely separate. The former includes a signal generation block that produces the oscillating signal injected inside the plant. A ring oscillator generates a square wave manually sent for the selected test period. The signal is injected on top of a tobacco plant and collected at the bottom thanks to two surgical needle electrodes spaced almost 40 cm from each other. On the other hand, a signal-conditioning module and a microcontroller unit comprise the receiving part, taking at input the attenuated signal that traveled inside the stem's plant. Specifically, the signal-conditioning module consists of a threshold comparator with hysteresis, whose feedback resistor is a digital potentiometer. By modifying the value of the potentiometer, the comparator's thresholds change until the signal's estimated amplitude is identified and related to the watering condition. This is made possible by the microcontroller unit, which communicates with the potentiometer via I^2C (Inter-Integrated Circuit) protocol and estimates the amplitude via a C routine. In addition, a special focus is given to the microcontroller's energy consumption by implementing its low-power modes. Lastly, the receiving system's output is sent to the PC through serial communication for appropriate analysis and correlations with the plant's water stress status.

The analyses were conducted in November 2022 on a tobacco plant with two water events. The choices in developing the architecture (in transmission and receiving) and the firmware parts resulted in a system capable of estimating the signal's peak-to-peak amplitude collected at the receiving electrode with good approximation and without the aid of the ADC. During the tests, it was observed that the signal voltage loss between the transmitting and receiving systems was maintained between $-18\,\mathrm{dB}$ and $-23.5\,\mathrm{dB}$. This leads to a percentage of attenuation of about 88% - 93.3%. Moreover, the correlation between the signal's peak-to-peak amplitude collected at the receiving electrode and the stem's impedance at the transmitting frequency showed that when the impedance in modulus decreases (a sign of proper irrigation), so does the peak-to-peak amplitude collected. However, this was observed only when irrigation occurred with a non-suffering plant state. Otherwise, irrigation in a condition of plant sickness leads to an opposite correlation: modulus increases while amplitude decreases.

The outcomes establish a foundation for indirect impedance measurement, understanding the plant's state with a simple, low-cost, and full-digital system. Nevertheless, more acquisitions are needed to create a reliable correlation model between the two electrical parameters analyzed, especially by observing the behavior of amplitude collected and impedance modulus with regular irrigations. Moreover, it would be useful to increase the number of plants analyzed to generalize the predictions to an entire category of plants.

Acknowledgements

Ringrazio il prof. Demarchi per avermi dato la possibilità di svolgere questo lavoro di tesi. Ho amato il progetto fin dal primo istante in cui mi è stato esposto. Un ringraziamento speciale va ai miei correlatori Umberto e Stefano; essere seguita passo dopo passo da persone competenti, disponibili e piene di passione come voi mi ha permesso di imparare tanto. Ho fatto tesoro di tutti i vostri consigli e vi ringrazio per avermi chiarito dubbi e incertezze ogni qualvolta ne avevo bisogno. Lavorare con voi è stato stimolante e interessante sotto ogni punto di vista e per questo non finirò mai di ringraziarvi. A voi, auguro tutto il meglio per il futuro.

Pongo un ringraziamento speciale, inoltre, a tutte le persone che mi sono state vicine negli anni.

Ai miei genitori, Dori e Claudia, per avermi insegnato cos'è l'amore. Il vostro continuo sostegno, la vostra premura e i vostri insegnamenti sono stati essenziali per farmi arrivare fino a qui. Questa tesi è dedicata a voi, il vostro amore nei miei confronti è il motore delle mie azioni.
A mio fratello Massimo, la tua dedizione e impegno nella vita mi ha insegnato che tutto si può raggiungere, basta puntare in alto. Nella tua singolarità, ci sei sempre stato. Per questo, e per altre ragioni di cui noi due sappiamo bene, ti ringrazio.
Ai miei nonni, Teresa, Franceschino, Assunta e Antonio, per avermi insegnato fin da piccola che basta poco per essere felici. Il vostro affetto mi segue sempre, ovunque io sia.
A tutti i miei amici, a quelli "di giù" e a quelli che ho conosciuto negli anni grazie al Politecnico. Tutti voi, nella vostra diversità, avete contribuito a rendermi migliore, ascoltandomi e consigliandomi. La vostra presenza nella mia vita è essenziale e vi ringrazio per farmi sempre ridere.
Per ultimo, ma proprio perché tanto importante vorrei ringraziare Francesco, che da quando l'ho conosciuto ha fatto splendere ancora di più il sole che ho detto. La tua dolcezza, intelligenza e pazienza mi toccano ogni giorno e senza di te molti problemi della mia vita sarebbero ancora irrisolti. I tuoi consigli, gesti e incoraggiamenti li porto nel cuore e non fanno altro che farmi brillare ancora di più. Per questo e per

altre infinite ragioni ti ringrazio.

Tutti voi avete contribuito a rendermi la persona che sono oggi. Vi ringrazio dal profondo del mio cuore.

Marta

Table of Contents

List of Tables

List of Figures

Acronyms

GHG

Greenhouse gas

IoT

Internet of Things

WSNs

Wireless sensor networks

DSS

Decision Support System

IBC

Intra-Body Communications

BCC

Body Channel Communication

PBCC

Plant Body Channel Communication

GC

Galvanic Coupling

CC

Capacitive Coupling

TX

Transmitting

RX

Receiving

PCB

Printed Circuit Board

RO

Ring oscillator

I2C

Inter-Integrated Circuit

SPI

Serial Peripheral Interface

MCU

MicroController Unit

Chapter 1

Introduction

The industrialization has often been the main factor in wealth and a better society. Still, research has shown that, while it does improve living conditions in some ways, it hurts the planet and inevitably contributes to global warming. The increase in population was one of the factors that led to urbanization, which in turn caused a rise in human activity worldwide. Human action's dominant role has resulted in two negative aspects: greenhouse gas (GHG) emissions and deforestation of huge global areas.

GHG are primarily composed of carbon dioxide (CO_2), methane (CH_4), and nitrous oxide (N_2O), and their levels have increased significantly as a result of the overuse of oil and coal, and natural gas. Figure 1.1 depicts the global average CO_2 (one of the leading greenhouse gases) concentration in the environment in the last 800.000 years, evaluated in parts per million (ppm). The graph shows that levels were stable until the 18^{th} century at 270 to 285 ppm. Following the Industrial Revolution, global CO_2 concentrations have continued to increase, surpassing 400 ppm, which is thought to be the highest in the last three million years [1].

Furthermore, as the population grew, so did the demand for land for urbanization and food production, which has led to deforestation. Figure 1.2 shows that 10.000 years ago, forests surrounded 57% of all habitable land on the planet (6 billion hectares) [2]. Only 4 billion hectares persist today, accounting for one-third of the globe's original forest area. In particular, when the world's population increased tenfold in 1700, the amount of land used for agriculture - land to grow crops and livestock grazing - increased [2].

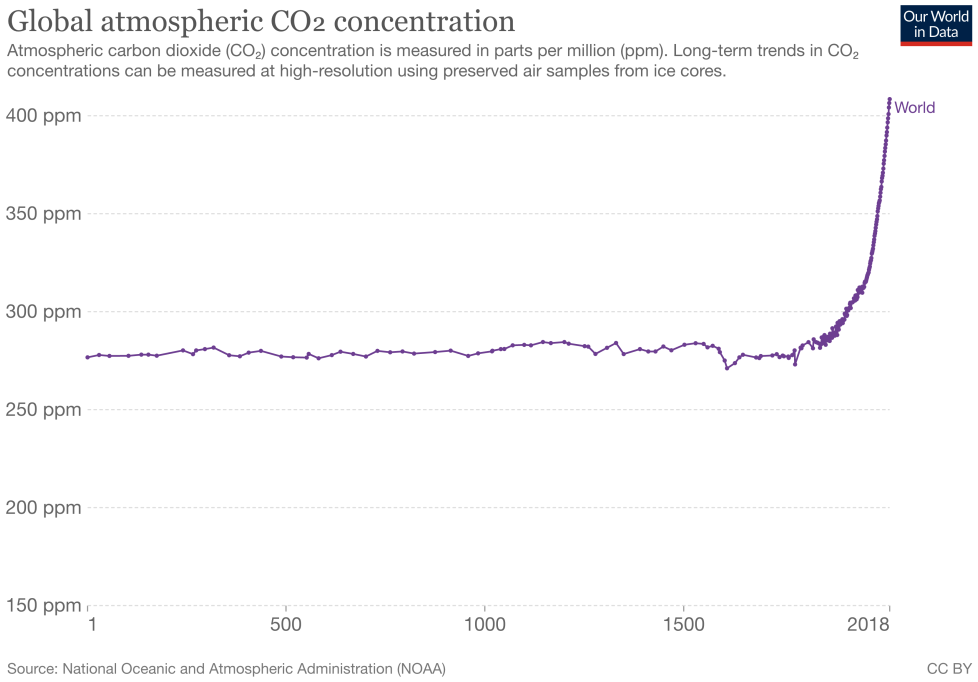

Global atmospheric CO2 concentration

Atmospheric carbon dioxide (CO_2) concentration is measured in parts per million (ppm). Long-term trends in CO_2 concentrations can be measured at high-resolution using preserved air samples from ice cores.

Source: National Oceanic and Atmospheric Administration (NOAA)

CC BY

Figure 1.1: Atmospheric carbon dioxide (CO_2) concentrations over the last 800.000 years, measured in parts per million (ppm) [1].

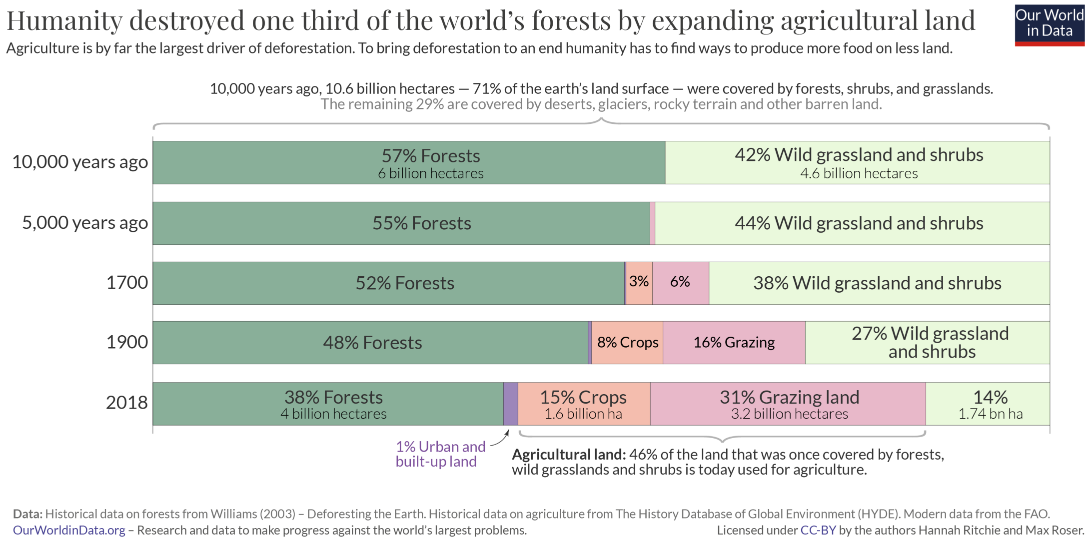

Humanity destroyed one third of the world's forests by expanding agricultural land

Agriculture is by far the largest driver of deforestation. To bring deforestation to an end humanity has to find ways to produce more food on less land.

Data: Historical data on forests from Williams (2003) – Deforesting the Earth. Historical data on agriculture from The History Database of Global Environment (HYDE). Modern data from the FAO.
OurWorldinData.org – Research and data to make progress against the world's largest problems. Licensed under CC-BY by the authors Hannah Ritchie and Max Roser.

Figure 1.2: Earth's surface changing over the past 10.000 years [2].

Agriculture's growth has been one of humanity's most significant environmental impacts, claiming responsibility for approximately 26% of global GHG emissions, as shown in figure 1.3 [3].

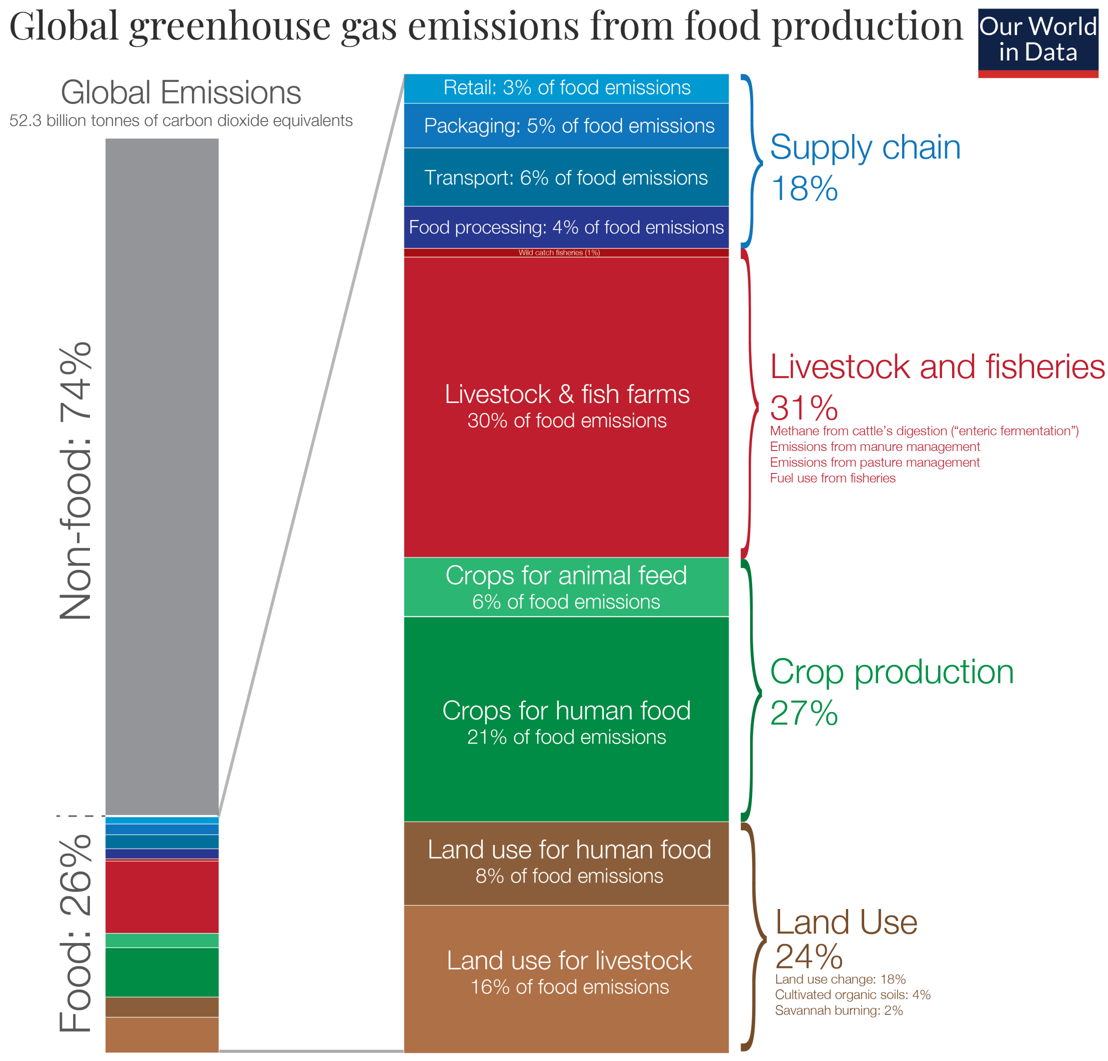

Data source: Joseph Poore & Thomas Nemecek (2018). Reducing food's environmental impacts through producers and consumers. Published in *Science*.
OurWorldinData.org – Research and data to make progress against the world's largest problems. Licensed under CC-BY by the author Hannah Ritchie.

Figure 1.3: Global greenhouse gas emissions from the production of food [3].

When attempting to evaluate food GHG emissions, four key elements must be considered [3]:

- **Livestock**: animals raised for meat, eggs, etc. contribute 31% of food emissions by emitting methane during their digestive processes.

- **Crop production**: crop production for human consumption contributes for 21% of food emissions, while animal feed production accounts for 6%.

- **Land use**: while emissions from human crop consumption are only about 8%, those from livestock land use are roughly double.

- **Supply chains**: 18% of food emissions are attributed to the conversion of farm produce into finished products, public transit, wrapping, and sales.

That is not all; to keep up with the world's rapidly growing population, farmers use fertilizers and pesticides, which has resulted in a 60% increase in agricultural emissions (CH_4) over the last 40 years [4], indicating a symbiotic relationship between emissions and agricultural output.

As energy and food demand rises, so does the demand for productive sites, where food and feed supply, biofuel, and urban growth compete. These issues are worsened by the gradual change in the ecosystem caused by human action, which has resulted in 1) rising temperatures on the planet, 2) melting glaciers and rising sea levels, 4) heat waves, droughts, and an increase in desert areas, 5) extreme natural phenomena such as floods, storms, hurricanes, and wildfires which are becoming increasingly common, 6) erosion, water stress, increasing soil salinity and 7) biodiversity loss on the planet [5]. Figure 1.4, obtained from the Berkeley Earth global temperature report, depicts the temperature variations in 2019, contrasted with those of 1951-1980 [1]. The average land surface temperatures rose about 1°C compared to the past, while the average sea surface temperature (except for regions of sea ice) increased by 0.6 °C. The map shows that certain regions underwent a more extreme temperature change, particularly in areas at higher latitudes (closer to the poles), reaching temperature anomalies over 5°C [1]. Unfortunately, these are often the areas that will be most affected by factors such as sea ice, permafrost, and glacial melting.

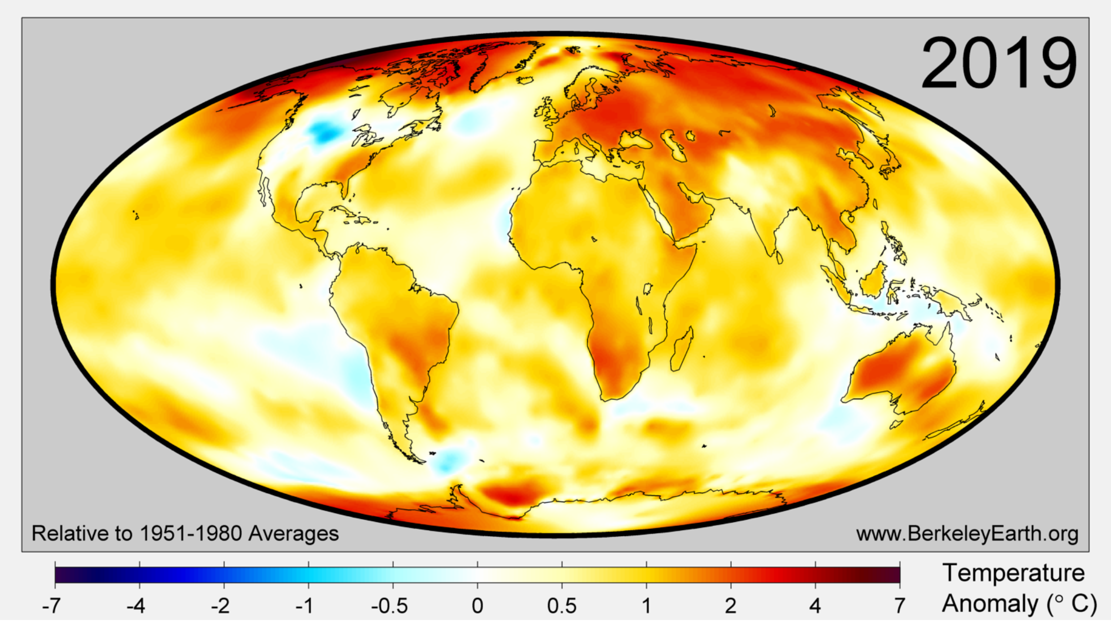

Figure 1.4: Local temperatures in 2019 relative to the average temperature in 1951-1980 [1].

Therefore, action must be taken to combat all the problems described above. Due to our activities, we have altered three-quarters of the terrestrial environment and more than 60% of the marine environment. The event that drives us the most to modify habitats is feeding ourselves by converting forests and grasslands to crops, and pastures [6]. Thus, a good starting point is to take care of the GHG emissions footprint left by humans in food production and consumption by developing new technological systems based on agricultural diversification, water resource conservation, and efficient land use while preserving biodiversity [4].

1.1 Smart Agriculture

According to global risk intelligence firm Verisk Maplecroft, by 2045, climate change will endanger more than 70% of the world's agriculture while the world's population is expected to rise to 9.5 billion. With current emissions rates and temperature increasing above industrial levels, agricultural production will be threatened in 64 countries by mid-century, up from 20 today ([7]). As a result, climate-smart methods known as Smart Agriculture or Smart Farming have been adopted in recent years, gaining traction at the national and international levels to meet the future challenges of agricultural planning. It refers to practices and methods that improve agricultural production, enhance adaptability to climate change, and reduce GHG emissions. Environmental variables, soil properties, water supply, and agrochemicals are just a few of the agricultural parameters that smart agriculture can monitor to improve yields and reduce costs [8]. Typically, it relies on the use of Wireless sensor networks (WSNs) in integration with the Internet of Things (IoT) [9, 10, 11, 12]. While WSNs track and collect physical conditions in real-time (such as temperature, vibration, or motion), IoT provides easy access to information gathered from sensors through the use of specific platforms [12]. Thus, the aim is to reduce resource consumption and environmental impact while increasing efficiency and quality by combining intelligent sensors and communication engineering with cloud storage.

In the next section, a brief overview of new technologies used in smart farming will be briefly introduced.

1.1.1 Brief overview

Technological advancements may enable humanity to boost food production in a greener way to meet sensible demands. In particular, to propel farming activities to new heights, these new technologies should address water, irrigation, soil, weather, nutrient (herbicides and pesticides), and waste management [9].

This subsection investigates articles in the literature that discuss cutting-edge agricultural technologies. It is divided into two macro-blocks: essays on environmental monitoring and reports on monitoring the plant itself.

Environmental monitoring

In [10], an implementation of a Long Range Wide Area Network (LoRaWAN) based smart agriculture Decision Support System (DSS) to optimize the yield is presented. This work aims to maximize profit while achieving sustainability by increasing per-hectare production and decreasing water leakage. The system described in this paper includes sensors for soil moisture, humidity, NPK (Nitrogen, Phosphorus, and Potassium), temperature, and pH and sends data to the cloud via the internet. The cloud-based development of logic-based DSS software considers accessible sensors' data, historical trends, and the influence of weather conditions. It provides recommendations and alerts as required for optimal yield for each site. The system also includes creating an app to assist farmers and landowners in monitoring their farms at any time and from any location.

In [13] an intelligent WSN-UAV(Unmanned Aerial Vehicles)-based IoT framework for precision agriculture is proposed. The use of aerial vehicles is one of the remote plant monitoring applications. Specifically, the paper's authors collected data on agricultural land using IoT smart devices and multi-rotor UAVs for aerial tracking and irrigating. Optimized UAV trajectories were investigated, with special emphasis placed on data processing technique, which effectively uses deployed WSN resources. All of this added up to a coverage efficiency of 96.3%.

Plant monitoring

Moreover, plant leaf variations are another area that is being monitored. The study in [11] demonstrates that evapotranspiration rates can be measured by comparing leaf temperature to air temperature. The sensor is attached to a leaf and is used to measure the leaf-to-air temperature differential to monitor plant water stress.

However, electron, proton, and dielectric transfer are involved in almost all plant life activities. Thus, plant electrical parameters are strongly linked to plant daily life, such as metabolism, growth, stress responses, etc., so they can be used to inspect its physiological state [14]. Because it is believed [14] that modifications in a plant's electrical characteristics are the quickest plant reactions to climatic factors, new approaches have emerged that investigate electrical impedance to characterize live plant stems. In [15], authors have demonstrated that the electrical stem's impedance increases when the plant gets dry and decreases when it is hydrated. It implies we can decide when the plant receives irrigated by measuring in situ plant stem impedance.

Since the crop and single-plant health tracking system is designed to provide continuous monitoring, the main challenge is to extend their life so that they can work independently for a long time. Typically, batteries are used for these applications given their low cost and low leakage. Still, they have one major drawback: a temperature change can lead to a risk of deterioration and reduced performance. Thus, energy harvesting sources such as solar energy, wind energy, environmental vibration, and so have been introduced. Nevertheless, the use of biomass as an energy source has recently been examined [16]. Specifically, Plant Microbial Fuel Cells (PMFC) is an excellent potential biotech that generates bioelectricity by utilizing microbial activity at plant roots (rhizosphere region). Microbial species in the soil around the rhizosphere degrade organics to produce electrons. PMFC takes advantage of this mechanism capturing electric charge produced by microbes in the anode zone. When electrons achieve a cathode, electricity is generated, known as "bioelectricity". As a result, the oxidation/reduction gradient among two electrodes causes electricity [16]. Figure 1.5 shows an explanatory image of how PMFC can be implemented. The setup includes two electrodes in a plastic pot: an anodic electrode placed in the rhizosphere region and a cathode at the bottom.

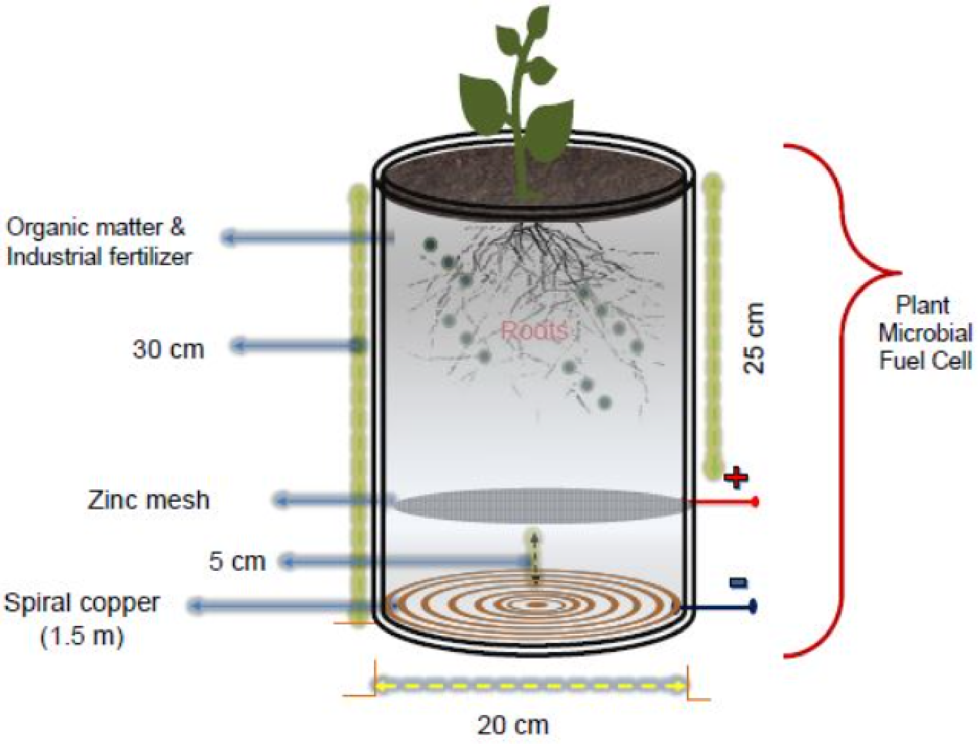

Figure 1.5: The PMFC proposed in [17] is depicted schematically.

1.2 Thesis organization

The motivations for developing this thesis were discussed, as well as the concept of Smart Agriculture. Instead, the current section explains how this thesis is divided up. In particular:

- Chapter 2 describes plant anatomy and signal transmission techniques found in the literature. Lastly, the final system will be presented.
- Chapter 3 deals with a thorough description of the system architecture. Components that are a part of it will be explained in detail, as well as how they were designed.
- The firmware application setup is shown in Chapter 4, focusing on the application code implemented to estimate the amplitude of the signal that has traveled inside the plant.
- Chapter 5 describes the real test performed and the results obtained.
- Chapter 6 will present the conclusions and possible improvements that can be implemented to improve performance.

Chapter 2

Signal transmission inside plants

The assessment of stress in plants is critical in agriculture, so proximity plant monitoring for crop and single-plant health has taken hold [15, 18, 19, 20, 21]. Standard methods use sensors to trace the health condition. In contrast, this thesis proposes an alternative approach to understanding plant health conditions by directly exploiting a signal injected into the plant's stem.

This idea was born taking into consideration works done on intra-plant communication [15, 18, 19, 20, 21] that took inspiration from biomedical applications. Hence, to understand how to study a plant, it can be possible to use measurement techniques developed for human bodies and investigate how appropriate they are for plant application. As a result, an explanation of Intra-Body Communications (IBC) methods is provided, illustrating that just as the body can be used to extract critical physiological variables, also a plant. Then, new approaches in intra-plant communication are presented in the literature, and the choice of the plant used in this thesis is explained.

2.1 Human Body Communications

IBC, also known as body channel communication (BCC), is a technique that employs the human body as a medium for signal transmission, allowing different devices, such as sensors, to connect with a single gateway. IBC techniques are classified into [22]:

- **Radio frequency (RF) based method**
  It is classified into two types: RF-Narrowband (RF-NB), which is utilized for remote patient monitoring and on-body and embedded sensor communication, and RF-Ultra-wideband (RF-UWB), which is used in implantable pacemakers

to communicate important data, such as cardiac rhythm wirelessly.

- **Ultrasound communication (US)**
  It is an acoustic-based method used in medical applications to transmit images and telemetry data from a device within the body to receivers outside the body.
- **Capacitive coupling (CC)**
  It is an electric field-based method. It is based on the energy transfer between one transmitter and receiver electrode to generate an electrical signal propagating through the human body. Capacitive coupling requires only two electrodes and an environment-based return path. The body acts as a potential electric conductor, and the ground serves as a signal return path.
- **Galvanic coupling (GC)**
  It is a waveguide-based method similar to capacitive coupling. The distinction between the two methods is that the alternating current is coupled within the body rather than between the body and the environment. The current propagates due to the ion content of the human body from the two electrodes in transmission to the receiving electrode pair.
- **Resonant coupling (RC)**
  It is a magnetic field-based method that generates a magnetic field throughout the body by utilizing the properties of electromagnetic resonance. Resonance coupling generates a near-field wireless transmission of electrical energy between two coils swathed around different body parts, which drives field propagation.

Figure 2.1 conceptually shows the path followed by the signal in the methods described above. Otherwise, the table 2.1 highlights their characteristic, particularly the maximum attenuation values correlated to the maximum link distance and the frequency ranges.

Table 2.1: Summary of IBC methods and main features [22].

IBC overview			
IBC method	Max.Attenuation[dB]	Max.Propagation Distance [cm]	Operating Frequency
RF-NB	80	20	401-406 MHz
RF-UWB	>80	12	3.1-10.6 GHz
US	100	10	1-100 MHz
CC	65	170	100 kHz-120 MHz
GC	65	15	100 kHz-10 MHz
RC	35	130	DC to 50 MHz

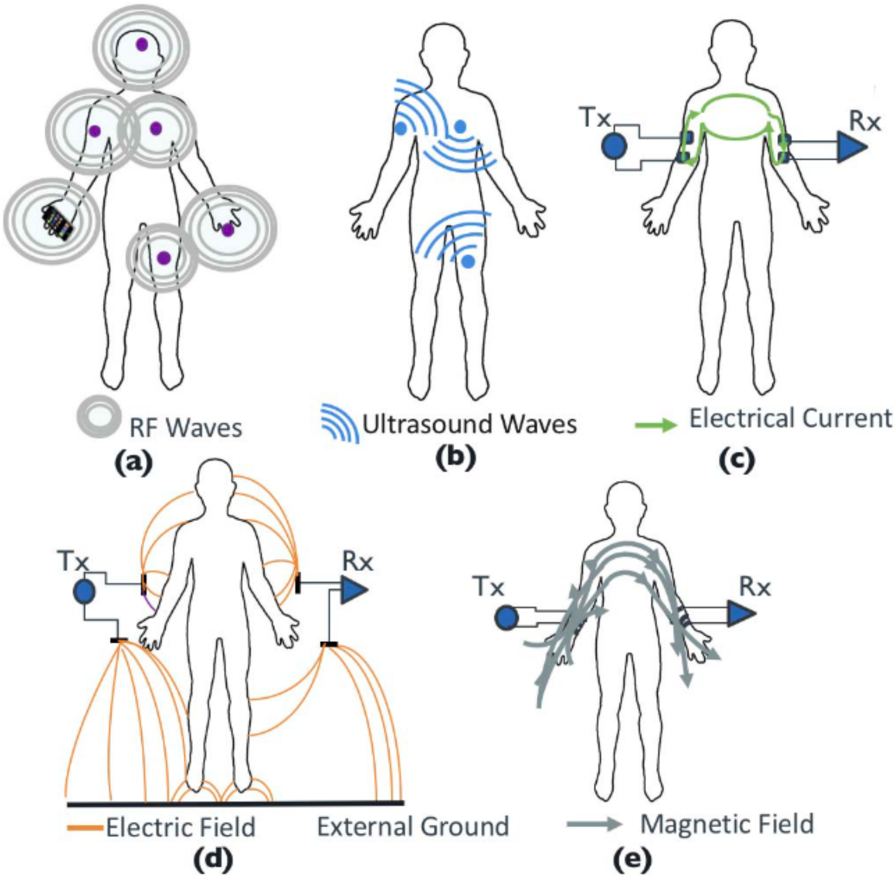

Figure 2.1: Conceptual diagram of (a) radio frequency, (b) ultrasound, (c) galvanic coupling, (d) capacitive coupling, and (e) resonant coupling. The imagine is taken from [22].

Among all the approaches, the galvanic coupling is the one that shows the most negligible attenuation of the signal about the maximum distance between the electrodes [22]. It has the added benefit of tissue safety and security (the signal is contained entirely in the body), consumes less power than wireless RF communication, and is more reliable than capacitive coupling. Moreover, the absence of wires makes it more comfortable and convenient for the patient. Thus, it's a widely used method that researchers are gradually trying to improve.

In [23] is presented a new GC-IBC architecture. The standard framework is typically composed of multiple embedded implants that send their sensed data to an on-skin node known as a relay. In contrast, this paper [23] proposes a distributed

beamforming (signal processing technique) approach that allows coordinated transmissions from the implants to the relays by taking into account the specific tissue path chosen as well as tissue heating-related safety limitations.
The simulation results show that implants improve network lifetime by up to 79% when compared to galvanic coupled links without beamforming [23]. When beamforming is enabled, coordinated transmissions increase received signal strength and SNR, resulting in the system's lower BER (Bit Error Rate) than individual transmissions. Figure 2.2 reports the bit error rate of the system related to one without beamforming: the system falls in the order of 4e -4, compared to 2e -3 for the scenario with no beamforming.

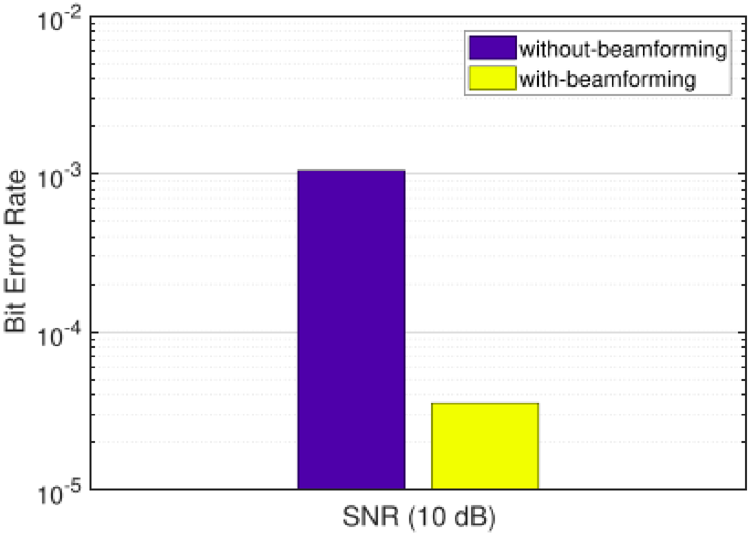

Figure 2.2: Result in terms of BER taken from [23].

2.2 Plant Body Channel Communication

Galvanic methods are commonly used in biomedical applications due to their simplicity in frequency constraints, reliability, and so on. However, because most of the current in galvanic IBC passes through muscle, it is expected that if these methods are used on plants, the current will pass through tissues from which the plant's stem is made. As a result, plant body channel communication (PBCC) approaches have been reported recently.

Aakash Jog et al. l [24] propose a feasibility study for PBCC. This study was conducted on Nicotiana tabacum plants, where four electrodes (0.5 mm gold wire) were galvanically coupled. The first two for the transmitter were installed at the top of the plant, and the other two for the receiver were placed at the bottom. Figure 3.4 reports the experimental circuit setup described above.

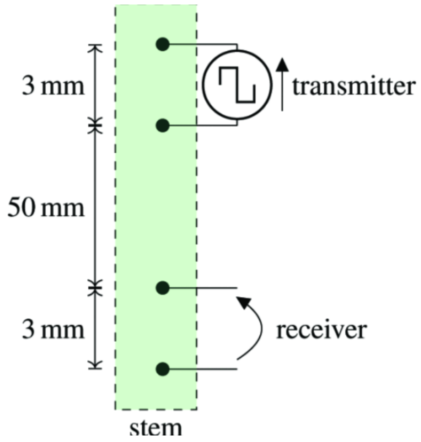

Figure 2.3: Experimental setup taken from [24].

Hence, rectangular pulses (0 V- 500 mV) with a 20% duty cycle and frequencies ranging from 100 Hz to 100 kHz were used as input to investigate the behavior of the stem as a transmission medium. The signal attenuation through the stems was studied in frequency and time domains. Since signal attenuation in BCC applications depends on transceiver symmetry (i.e., electrode configuration), the goal is to see if the same dependence exists in PBCC. The electrode pair, TX and RX, has one source and one ground electrode, and they have been inverted to generate four different transceiver symmetries. The output pulse shapes and input/output RMS voltage attenuation were investigated for each configuration.
In this work, it has been found that the mean swing (i.e., the mean difference between the minimum and maximum values) of the gain values is 3.515 dB, which is comparable to that observed in human BCC for the same frequency range [24].

Also, the gain varies significantly between four transceiver configurations, but it has not been determined whether one is better. Furthermore, the authors wanted to emphasize how the received pulse's shape depends on the input's pulse amplitude and frequency.

Plant stem was also used as a communication channel by the authors of [21] to investigate PCCB. Two pairs of electrodes, one for transmitting (TX) and one for receiving (RX), are inserted into the plant stem of a Prunus Bianco with a stem diameter of 3 cm, separated by a channel length 1 cm. It should be noted that the electrodes in TX and RX were oriented in such a way that they faced each other. Specifically, when the first electrode is positioned, the second is oriented 180 degrees to the first, both located in the same plane.
In figure 2.4, the three investigated setups based on grounding strategies are shown:

1. Earth Grounded
2. Balun transformer in TX
3. Battery-powered

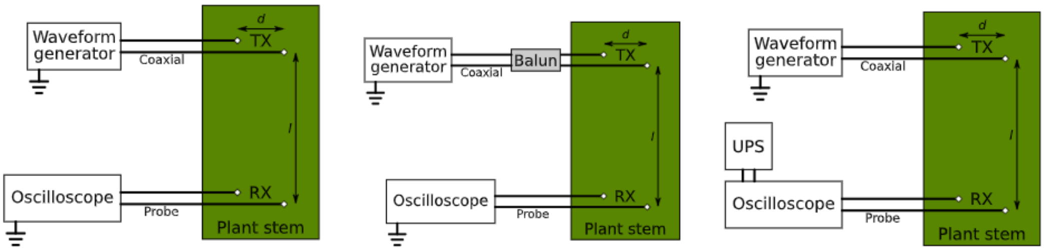

Figure 2.4: Block diagrams of different grounding strategies' experimental setups for galvanic coupling transmission examined in [21].

The signal to be injected (TX) was generated by an arbitrary waveform generator (AWG) with coaxial cable, with an amplitude of 3.3 V and a frequency range consisting of 19 logarithmic spaced points between 10 kHz and 1 MHz. Specifically, channel characterization was performed using electrodes of varying distances and lengths, as well as the calculation of voltage loss, found via the formula 2.1:

$$Gv(dB) = 20log_{10}(V_{RX}/V_{TX}) \tag{2.1}$$

where G_v is the voltage loss in dB, V_{TX} and V_{RX} are, respectively, the received and transmitted peak-to-peak voltages.
The results of the tests performed have yielded the following outcomes:

- **Setup characterization for different grounding strategies with *l = 20 cm*, *d= 1 cm***
  Results show that a battery-powered setup is the best option among the three because it eliminates measurement artifacts. Specifically, with this configuration, it was found the lowest voltage loss G_v of -21.6 dB (non-hydrated case) and -22.0 dB (hydrated case) at 100 kHz.

- **Battery-powered setup with three different channel lengths *l* of 5, 10, and 20 cm and *d = 1 cm***
  At 100 kHz, the lowest voltage loss G_v of -15.8 dB and -18.1 dB were found for *l = 10 cm* e *d= 5 cm*, respectively, with a frequency-averaged attenuation increase of -0.41 dB/cm.

- **Battery-powered setup with three different distances *d* of 1, 2 and 3 cm and *l = 20 cm***
  At 100 kHz, the lowest voltage loss Gv is -19.5 dB and -18.0 dB for d = 2 cm and d = 3 cm, respectively, indicating an attenuation decrease of 1.5 dB/cm.

As a result, because all measurements show a peak voltage loss of around 100 kHz, an optimum transmission frequency between 60 and 140 kHz is suggested.

2.2.1 Direct bio-impedence measurement

The electrical characteristics of a plant's stem can be associated with its health status. Electrical impedance spectroscopy, in particular, has been proposed as a plant sensing method in [15], referring to watering or moisturizing status. Figure 2.5, taken from this article, depicts an unwatered tomato plant whose impedance (modulus and phase angle) is calculated at 1 kHz. In particular, from figure 2.5a, it can be seen that as soil moisture levels decrease to complete saturation of the sensor ($-200\,\mathrm{kPa}$), the modulus of impedance increases to over tens of kΩ. Otherwise, in a watered plant, a value of the impedance modulus was found to range between 1.7 and 2.2 kΩ. A significant variation is also found in the impedance angle. When the soil is dry, this value decreases to -28 deg, in contrast to the -20 deg found under watering plant status.
Thus, impedance variations reveal a direct relationship with watering events, indicating plant watered conditions.

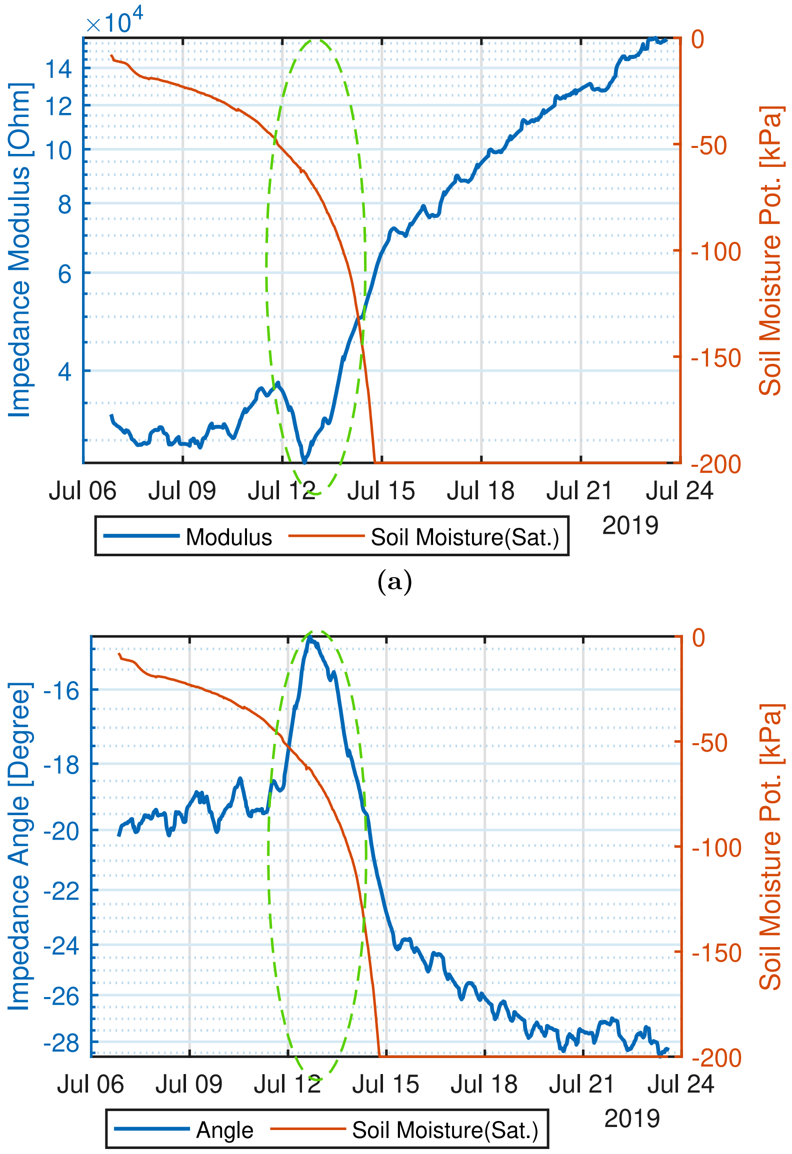

(a)

(b)

Figure 2.5: Electrical impedance of an unwatered tomato plant at 1 kHz from [15]. (a) Modulus of impedance and (b) relative angle.

This breakthrough led the authors in [19] to concentrate on the relationship between the stem electrical impedance and a day cycle. In particular, they demonstrated how the impedance at 10 kHz, in terms of modulus and phase, varies during the day according to environmental conditions. At noon, when the maximum brightness peak is reached, a modulus and angle of about 21 kΩ and -41 deg are recorded, while around 8 p.m. the values change to 24 kΩ and -39 deg respectively (see figure 6 from the article [19]). Thus, when the light conditions are optimal, a decrease in modulus and phase is recorded as opposed to its increase in the evening or early morning.

2.2.2 Indirect bio-impedence measurement

Studies conducted on the plant stem as a communication channel and the discovery of the relationship between impedance and plant water status set the stage for a new long-term goal: remove all environmental sensors and rely solely on direct measurement of plant parameters, eventually placing sensors directly on the plants themselves. This reduces costs, resulting in a more compact device.
As a result, the goal of this thesis is to develop a system that can indirectly measure the impedance-water-state relationship. The idea is to study the variation of a signal injected on top of a tobacco plant stem and collected at the bottom thanks to two surgical needle electrodes placed 40 cm from each other. The variation in the amplitude of the signal that traveled through the plant should correlate with its water needs, allowing its health status to be tracked.

2.3 Tobacco plant choice

Since the thesis work involves using the stem of a plant as a communication channel, one had to be picked first. The choice fell on the tobacco plant since it's very hardy, easy to grow in the laboratory, and its genome has been sequenced. Specifically, Nicotiana tabacum, with a stem diameter of 0.7-1 cm and a length of approx 0.7-1 m, has been chosen.

2.3.1 Conductive channels of vascular plants

Tobacco is part of the category of vascular plants, distinguished by the presence of fluid-conducting structures within them: the xylem (Xy) and phloem (Ph). The xylem transports salts and water absorbed at the root level to the leaves to enable the reaction of chlorophyll photosynthesis. In contrast, the phloem is a complex of living tissues with the functions of transporting refined sap (obtained as a result of photosynthesis), energy reserve, and transporting proteins and mRNAs required for survival and development [25]. Thanks to these pre-existing conductive channels in the plant, injected electrical signals can be transmitted [18]. Figure 2.6a shows the cross-section of a tobacco plant stem with the black arrow indicating the vascular cambium. This is located between the pith and cortex; its cells are divided to form a phloem (on the outside) and xylem (on the inside), as highlighted in figure 2.6b.

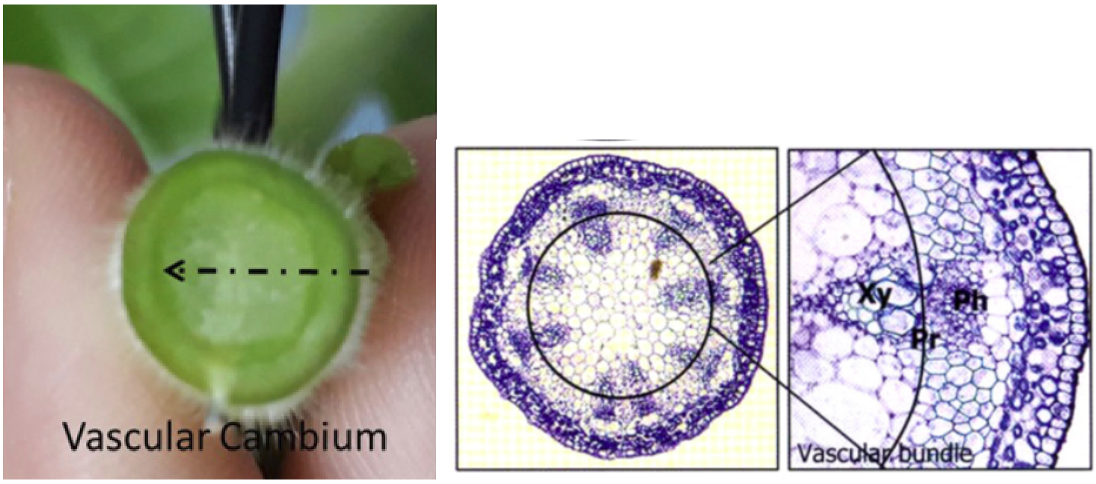

(a) (b)

Figure 2.6: Description of the cross-section of the plant stem. (a) Image of a real tobacco plant from [15]. (b) Cross section of a typical vascular plant as seen from the microscope from [25].

2.3.2 Electrical Connection to the Plant

For the thesis, sterilized needles are utilized as electrodes to transmit the signal inside the plant and pick it up after it has traveled into the stem. Using such electrodes should prevent oxidization because they are made of stainless steel, as reported in [26].

Electrical coupling to the plant stem was performed as follows: one needle was placed at the top of the plant and a second needle near the roots, separated by a distance of 40 cm. This distance was chosen as a compromise and to form the basis for a device capable of monitoring the health of taller plantations or even trees. During coupling, direct contact with the vascular cambium occurs and thus with water and nutrient conduction channels.

Moreover, it is essential to underline that for the entire period of the thesis, the same plant and a specific stem of it were used to maintain consistent experimental conditions.

Chapter 3

System architecture

This thesis proposes an alternative approach to understanding plant health conditions by directly exploiting a signal that has been injected into the plant's stem. It involves a low-cost device that aims to estimate stem impedance by monitoring the attenuation of a signal injected within the plant. It consists of a transmitting (TX) and a receiving (RX) system designed to have the following features:

- **Different ground for TX and RX**: transmission and receiving are designed to be completely separate systems. This would allow TX and RX to be placed as far apart as possible between them in the future and used with crops with stems longer than 1 m. Perhaps a similar system could be used to assess the health of trees.
- **Avoid using ADC (Analog-to-Digital Converter)**: although the ADC allows the amplitude value to be calculated effectively, this block was omitted. Avoiding the signal's analog reading reduced power consumption and a simpler overall system, as an additional conditioning module could be omitted.
- **Low-cost**: unlike common smart agriculture devices made up of customized and expensive sensor technology, this system presented uses components already on the market.

The following paragraphs explain the system in detail. Section 3.1 deals with the transmission system, while section 3.2 focuses on the receiving system. Moreover, component choices and calculations for their sizing are reported.
Finally, in section 3.3, the complete system is presented.

3.1 Transmitting system

Since the final device must be placed in the fields, it must be equipped with an autonomous power system. This thesis work uses a PCB (Printed Circuit Board)

designed by Barezzi [27] to power the device that is responsible for injecting the signal into the plant.
The following sections will explain the two transmission system components: the power and the signal generation block.

3.1.1 Power block

The front and back of the PCB developed in [27], which was used as the transmission's power source, is shown in figure 3.1. Figure 3.1a shows a SAFT model battery known as LS14500, which supplies energy to the PCB. It consists of LiSOCl2 (lithium thionyl chloride), which has lithium metal as an anode and thionyl chloride (SOCl2) as a cathode. Although it falls into the category of non-rechargeable battery, it was chosen for its low leakage and cost, allowing it to cover large plots of land [27]. This battery has a typical operating voltage of 3.6 V, AA size, and a discharge capacity of 2.6 A/h. Figure 3.1b shows the pins V+ and V- squared in red; between them, there is a voltage of 3.3 V when the battery is in full charge. This is made possible by including the 3.3 LDO Voltage Regulator block that guarantees a working voltage of 3.3 V with respect to 3.6 V as the input voltage [27].

(a) **(b)**

Figure 3.1: Photo of the PCB designed by [27].

3.1.2 Ring Oscillator

The device that generates the signal to be injected into the plant stem is a ring oscillator (the electrical connection to the plant is described in 2.3.2).
The ring oscillator (RO) used is a single-ended type, made up of an odd number of NOT ports connected in a ring where the result of the last gate is fed back into the first. However, because it is a single-ended architecture (voltages are referred to as a single point), it is susceptible to common mode noise, particularly supply voltage ripple and noise in the substrate. An example of one of its schematic structures can be seen in figure 3.2.

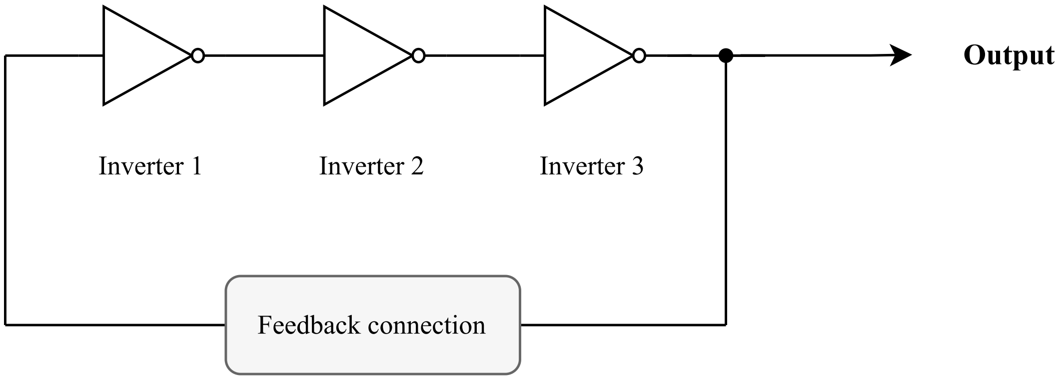

Figure 3.2: Example of ring oscillator's schematic structures.

Since the NOT port inverts the signal at its input (the output will be 1 if the input is 0 and 0 if the input is 1), the last output of this chain is the logical NOT of the first input. As a result, because the output is either high or low, this configuration will produce a square wave with a 50% of duty cycle and a peak-to-peak voltage equal to the power supply. However, this configuration does not allow the oscillation frequency to be controlled as it depends on the supply current and voltage, as well as the feedback resistance [26].

For this thesis, a 74HC04 made by Diodes Incorporated is used. Work done in [26] points out that the use of this device absorbs a small amount of current to work properly and thus allows the transmission block to last longer. Moreover, it's inexpensive because it consists of only two transistors for each NOT port.
The 74HC04 device provides six inverting gates, consisting of 14 pins as shown fig.3.3, where V_{CC} is the supply voltage, GND is the ground (0 V), and the letter A represents the NOT input, and the letter Y stands for the output.

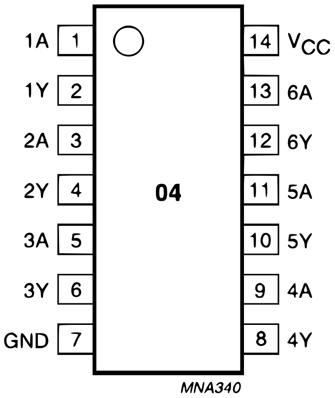

Figure 3.3: Pin configuration of 74HC04 component taken from its datasheet.

The operating conditions from the datasheet regarding supply voltage have a minimum value of 2 V and a maximum value of 6 V. The V_{CC} used for this application is 3.3 V, which is provided by the PCB described in the previous subsection. Furthermore, the feedback used to connect the sixth and first inverters is a simple jumper cable. The schematic structure described is depicted in 3.4, with a series of five NOT ports connected in a loop and a sixth used as a driver.

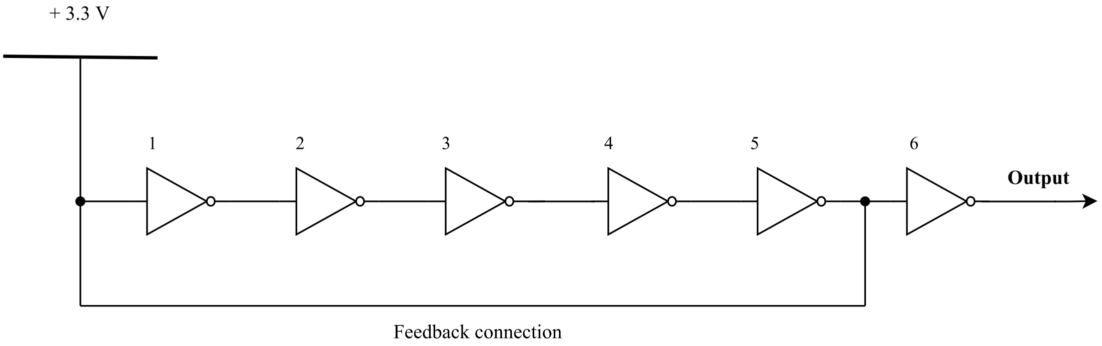

Figure 3.4: RO arrangement.

Moreover, backup capacitors Cbp_1 and Cbp_2 by the value of 1 μF and 4.7 μF, respectively, were connected between the supply voltage and ground to ensure that V_{CC} is stabilized (fig.3.5).

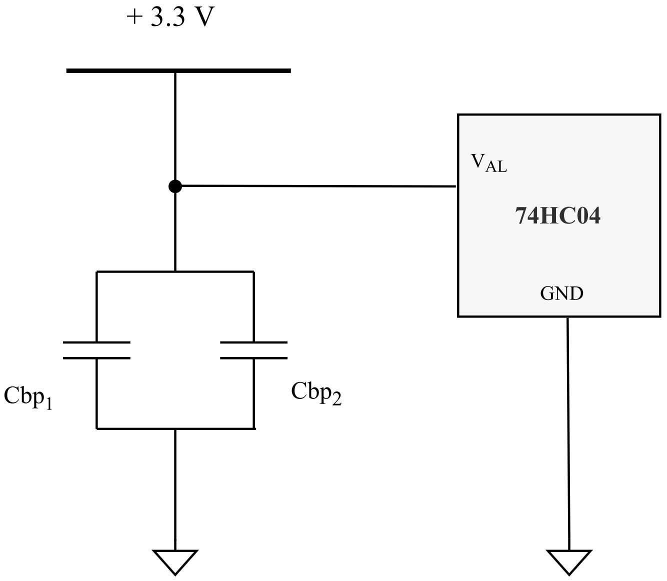

Figure 3.5: RO power supply with two bypass capacitors between the supply voltage and ground to mitigate the effect of low-frequency noise.

After defining the setup, the delivery frequency to the plant was chosen. Thus, bypass capacitors were added between the input of several inverters and the ground, allowing the voltage at the drivers' output to be slowed down to the desired frequency. Several frequencies between 1 kHz and 150 kHz were investigated (the range was chosen considering the literature work [15, 21, 18, 19, 20]), with a distance of 40 cm chosen between the TX and RX electrodes.
The tests were carried out as follows: the output of the ring oscillator powered as previously described was connected via an alligator cable to the electrode at the top of the plant while the probe of a portable oscilloscope (Fluke ScopeMeter 190-204) was directly connected to the second electrode at the bottom. The receiving signal at different frequencies and in different states of the plant (both hydrated and non-hydrated) was observed, and it was noted that:

- the same injection frequency was found at the bottom;
- for frequencies around hundreds of kHz, the square wave was distorted;
- for frequencies on the order of a few tens of kHz noise injection was so excessive that square wave analysis was not possible;
- for frequencies between 70 and 80 kHz, the observed square wave had a good trade-off between signal distortion and noise.

Figure 3.6 highlights what was previously reported. Each screenshot of the resulting RX wave was taken through the portable oscilloscope with a distance of 40 cm between electrodes. From fig.3.6a and fig.3.6c, it can be seen that when the frequency of the transmitted wave is 4 kHz, the wave is noisy, while when the frequency is 140 kHz, the wave is distorted.

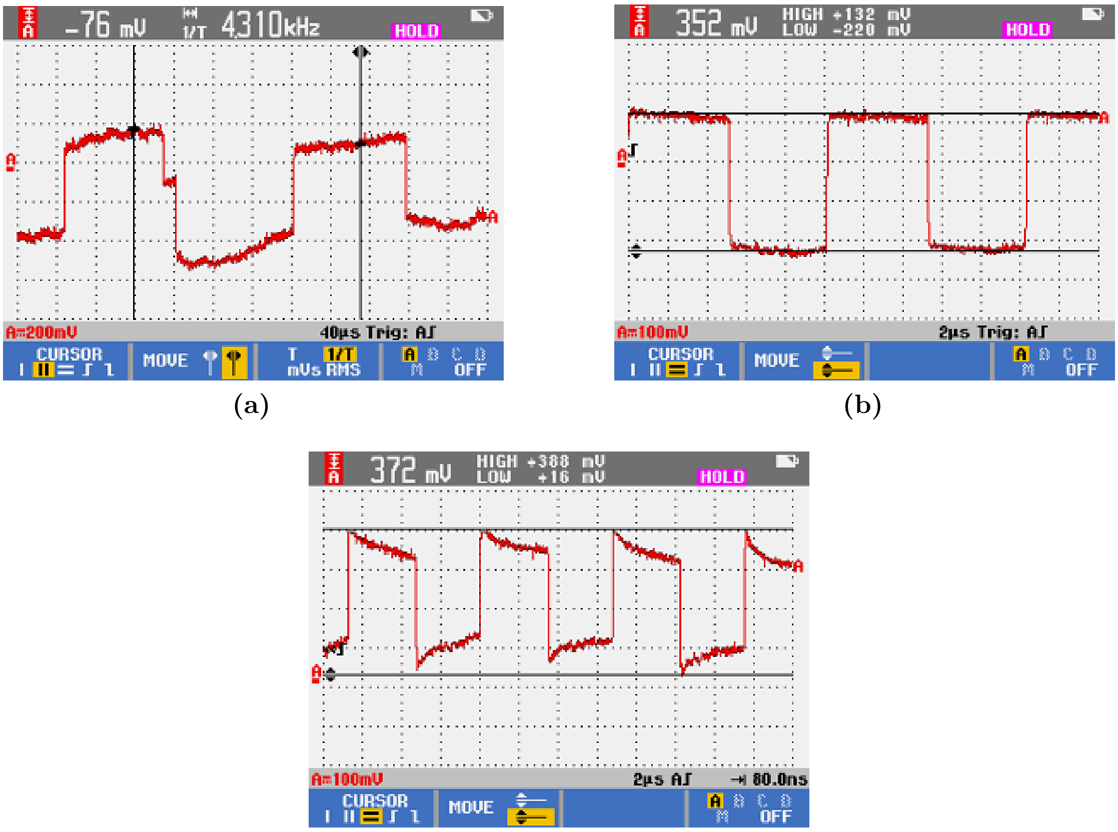

(a) (b)

(c)

Figure 3.6: Screenshot of the result RX wave, taken through the portable oscilloscope with a distance of 40 cm between electrodes. Fig.3.6a, fig.3.6b and fig.3.6c indicate the RX wave when the frequency of the transmitted wave is 4 kHz, 80 kHz, and 140 kHz, respectively.

Given the previous analyses, a frequency of about 80 kHz was chosen to conduct this thesis study. The resultant square wave is shown in 3.8 where fig.3.8a shows the peak-to-peak amplitude of the square wave in V, while fig.3.8b depicts the chosen frequency. Both screenshots were taken from the portable oscilloscope Fluke ScopeMeter 190-204.
To achieve this frequency, the following components were added (see table 3.1):

Table 3.1: Components utilized in the signal generation block.

Component	**Value**	**Type**
C_1	10 nF	Ceramic
C_2	47 nF	Ceramic
C_3	47 nF	Ceramic
C_{bp1}	1 μF	Electrolytic
C_{bp2}	4.7 μF	Ceramic

The final ring oscillator setup appears in figure 3.7.

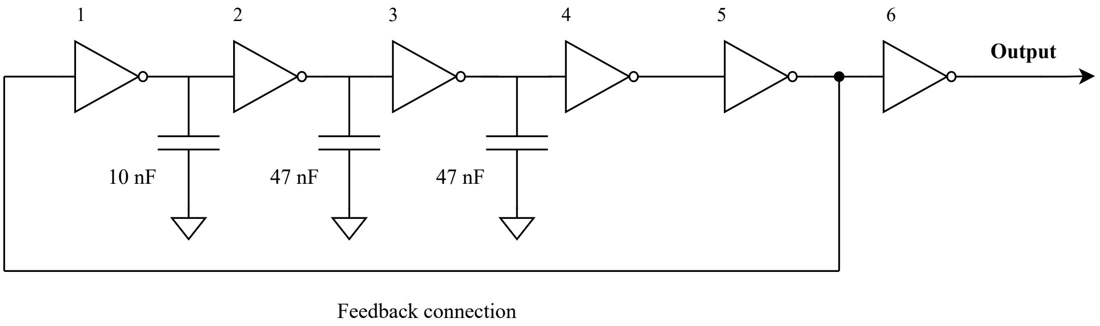

Figure 3.7: RO final arrangement.

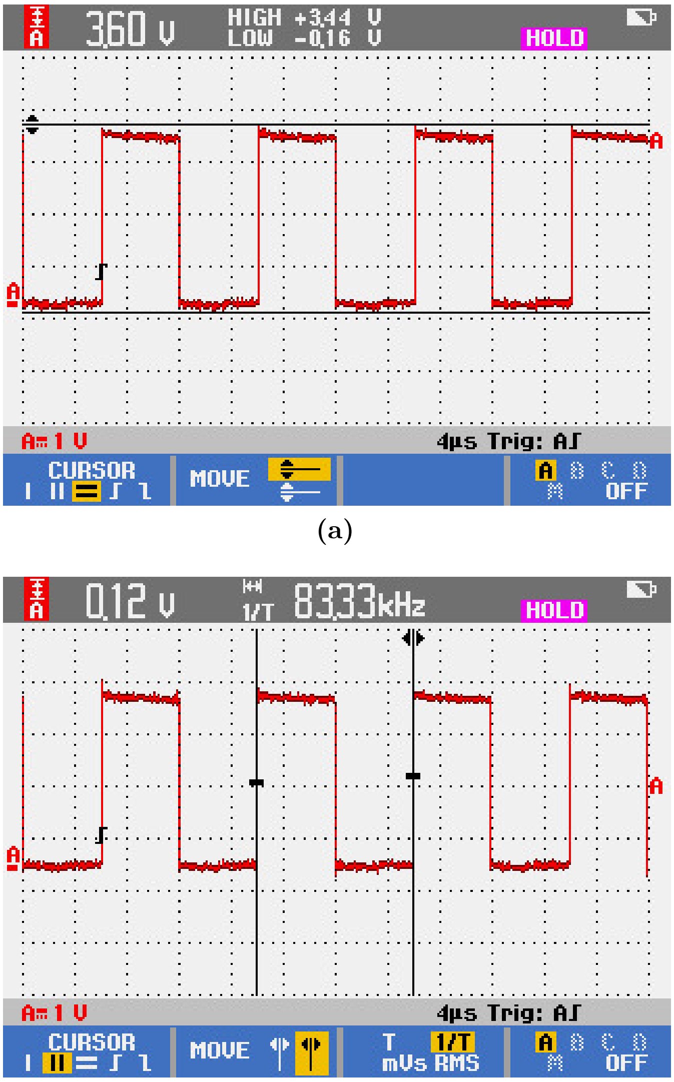

(a)

(b)

Figure 3.8: Screenshots of the resultant square wave taken through the portable oscilloscope present in the laboratory. (a) Peak-peak amplitude (b) frequency of the signal.

3.2 Receiving system

The previous section discussed the transmission part of the device developed in this thesis work. In contrast, this section deals with describing the receiving part. It is made up of a signal-conditioning module and a microcontroller unit. Specifically, the STM32 is the microcontroller mounting on a Nucleo Development board (Nucleo-F401RE) that receives the attenuated signal that travels inside the stem's plant as input. Since the ultimate goal of the device is to estimate the amplitude of the received signal, these two blocks must act simultaneously through a combination of firmware and hardware. Moreover, it is important to note that the supply voltage of the first block is given by the Nucleo-F401RE, which takes voltage from the PC via a standard USB-A port (details will be explained in subsection 3.2.2). Therefore, whenever a V_{CC} supply voltage equal to 3.3 V is seen in the figures for the signal conditioning block, it is derived from the Nucleo-F401RE.

The subsection 3.2.1 describes the signal-conditioning module while 3.2.2 describes the microcontroller unit. Each block's component will be explained separately to enable the reader to understand the final device's functioning.

3.2.1 Signal-conditioning module

Because the injected signal is attenuated once it enters the plant, it must be conditioned to facilitate its analysis. This module must also be applied to evaluate the RX signal's amplitude as a digital measurement.

The signal-conditioning module consists of an inverting threshold comparator with hysteresis, whose feedback resistor is a digital potentiometer. By modifying the value of the potentiometer, the comparator's thresholds (high-to-low transition and low-to-high transition voltage) changes until the signal's estimated amplitude is identified.

The digital potentiometer will be discussed first, followed by the comparator.

Digital potentiometer

The digital potentiometer selected in this thesis work is the AD5272, produced by Analog Devices. It uses an I^2C (Inter-Integrated Circuit) protocol, single-supply operation ranging from 2.7 V to 5.5 V, a 1024 position resolution, and a $50\,\mathrm{k}\Omega$ full-scale resistance. Furthermore, it has a maximum nominal resistor tolerance error of ±1%. Figure 3.9 shows the AD5272 functional block diagram, while figure 3.10 illustrates the pin configuration (both pictures were taken from the datasheet).

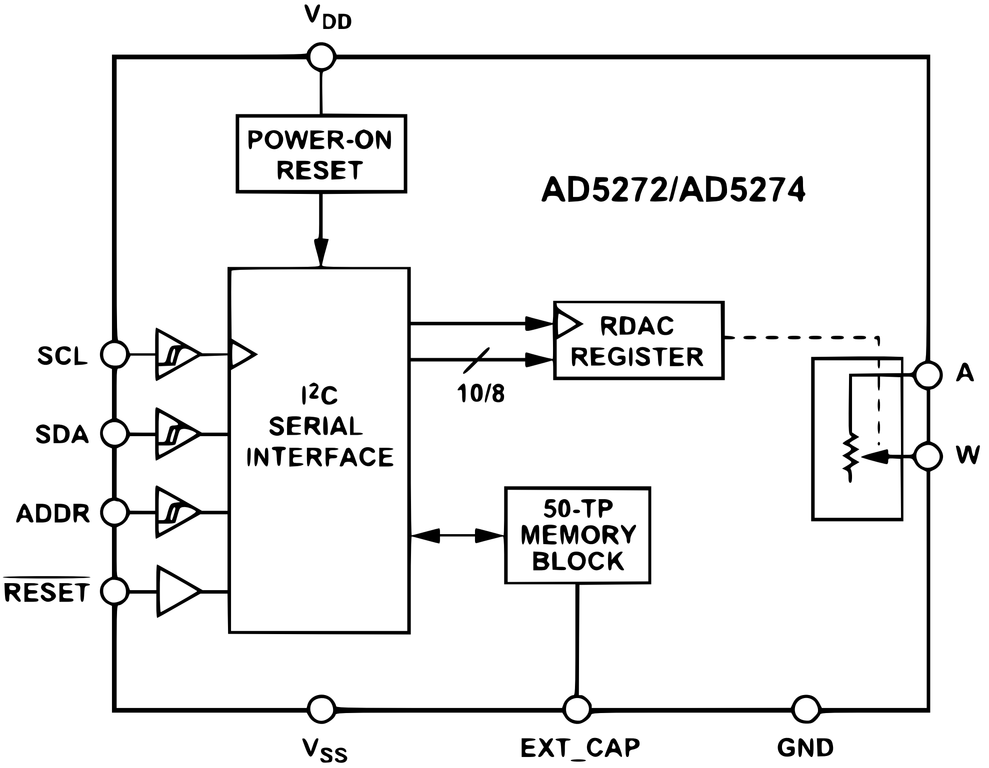

Figure 3.9: AD5272 functional block diagram obtained from the datasheet.

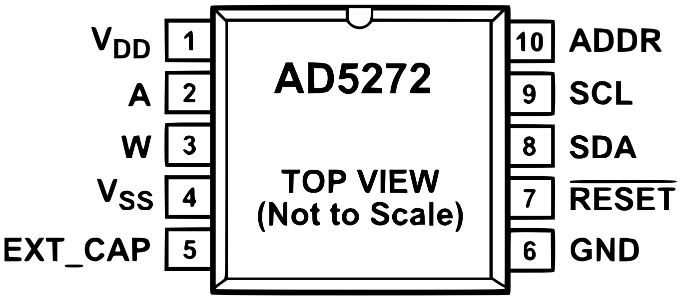

Figure 3.10: AD5272 configuration pin taken from the datasheet.

Referring to the previous figures, it is necessary to explain the following:

- **SCL - SDA**: serial clock (SCL) and serial data (SDA) are the lines that allow communication in I^2C. While SDA is the line dedicated to transferring/receiving the data, SCL is in charge of timing the data. In this work, an I^2C speed of 100 kHz (standard mode) is utilized.

- **ADDR**: ADDR pin status sets the two least significant bits (A0 and A1) of the 7-bit slave address. Table 3.2 is illustrative of the address the digital potentiometer assumes, based on whether the ADDR is connected to ground GND, power V_{DD}, or had no connection.

Table 3.2: Digital potentiometer address selection from its datasheet.

ADDR	**A1**	**A0**	**7-bit Address**
GND	1	1	01011**11**
V_{DD}	0	0	01011**00**
No connection	1	0	01011**10**

In this work, ADDR is connected to the ground; thus, the device turns out to have an address of 47 (decimal number).

- **RDAC register**: the content of the 10-bit RDAC (Resistive Digital-to-Analog Converter) register determines the position of the wiper (W in fig.3.9), which leads to defining the value of the resistor between terminal A and W, called R_{AW}. Specifically, if the content of the RDAC register is all 0, the wiper is located on terminal A. As mentioned earlier, the wiper can move 1024 positions and can be changed via the I^2C digital interface. The equation for calculating R_{AW}, as written in the datasheet, is:

$$R_{AW}(D) = \frac{D}{1024} \times R_{nom} \tag{3.1}$$

Where D is the decimal equivalent of the binary code loaded into the register and R_{nom} is the full-scale resistance equal to 50 kΩ.

An observation should be made: since the 50-TP memory block is not used in this work, it is not described.

The schematic circuit of the digital potentiometer is shown in figure 3.11. In this latter figure, C_1 and C_2, connected between the power supply and ground, are bypass capacitors, C_3 is the capacitor between EXT_{CAP} and ground and R_1 and R_2, connected between SCL and V_{CC} and SDA and V_{CC} respectively, are pull-up resistors. From fig.3.11 it can also be seen that R_{AW} is connected to the inverting comparator (a fuller explanation will be given in the next subsection).

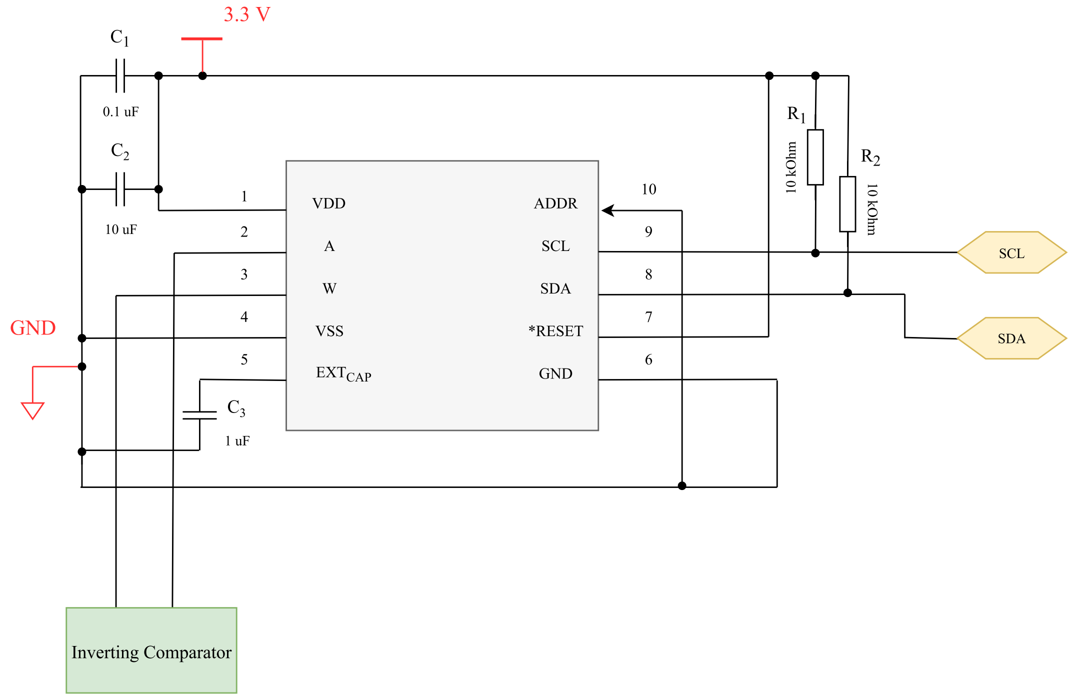

Figure 3.11: AD5272 schematic circuit.

The potentiometer resistance between pins W and A was changed by programming Nucleo-F401RE, following the datasheet's instructions.

Further investigation was carried out to determine the time (wiper settling time) it takes for the potentiometer to write to the RDAC register and move the wiper to display the correct resistor value, as it was not specified on the datasheet. This was done to decrease as much as possible the power consumption of the Nucleo-F401RE that powers the AD5272.
Analyses were conducted by programming, one at a time, the wiper to move in steps of $500\,\Omega$, $4\,k\Omega$, $20\,k\Omega$, and finally to jump directly from the first position to the last ($50\,k\Omega$); the movement of the steps was done in both ascending and descending order. Figure 3.13 shows a screenshot obtained from the RIGOL MSO5074 oscilloscope when the change in resistance was set to $50\,k\Omega$. Oscilloscope channel 1, in yellow, represents the output voltage from the partition between pin W and A. Figure 3.12 shows in orange the circuit for obtaining this partition (the right side of AD5272 has been omitted since it is not essential for the explanation). In contrast, oscilloscope channel 2, in light blue, represents a signal from one of the GPIOs of the Nucleo that is set to logic high before the write command and is set to logic low after writing. The difference in time between the GPIO signal going up (indicating the start of the writing in the RDAC register) and when the

partition goes down (representing the end of the write) is the wiper settling time.

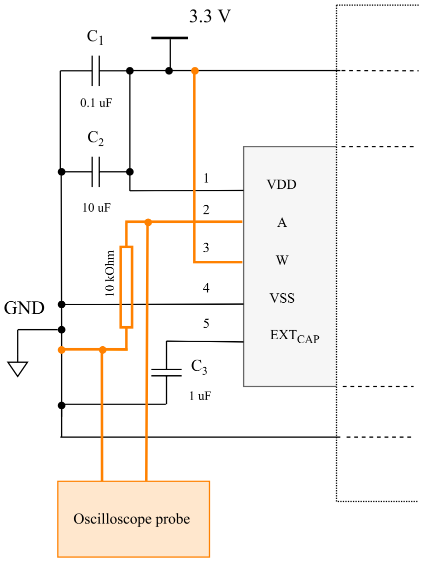

Figure 3.12: Circuit (orange) prepared for calculating the wiper settling time (the right side of AD5272 has been omitted since it is not essential for the explanation).

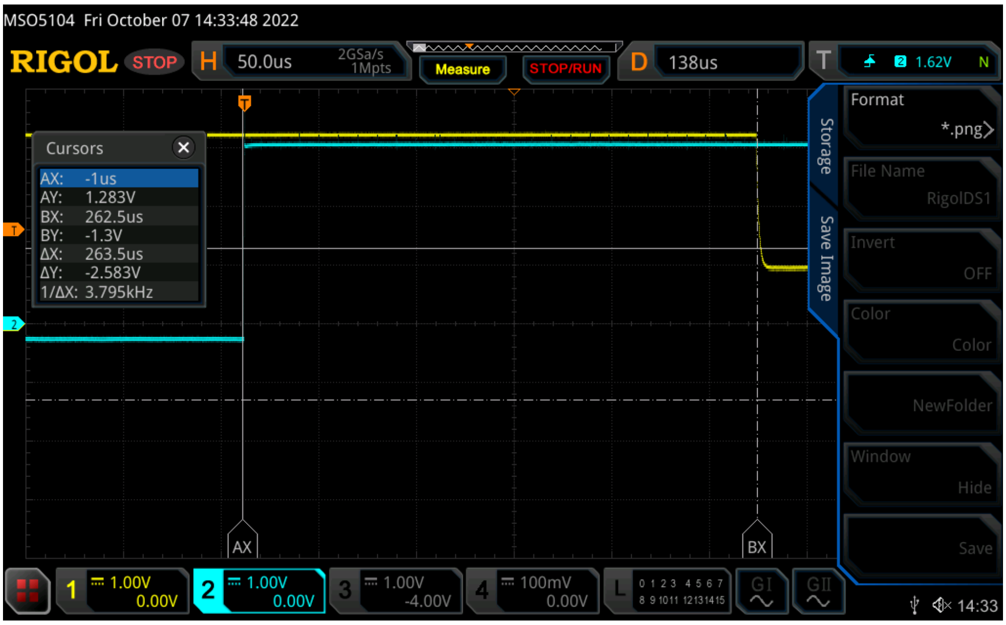
```
MSO5104  Fri October 07 14:33:48 2022
```
```
Cursors
AX:     -1us
AY:     1.283V
BX:     262.5us
BY:     -1.3V
ΔX:     263.5us
ΔY:     -2.583V
1/ΔX:   3.795kHz
```

Figure 3.13: Screenshot from the RIGOL oscilloscope when the resistance change was set to 50 $k\Omega$. The wiper settling time is $\Delta X = 263\,\mu s$.

Regardless of the change in resistance, the wiper settling time is maintained around $263\,\mu s$. This time is relatively small to allow low consumption.

The details of how AD5272 was programmed will be illustrated in the firmware chapter (subsection 4.2.3).

Threshold comparator

The Texas Instruments TLV7011, shown in figure 3.14 (picture taken from [28]), was chosen as the operational amplifier of an inverting comparator with hysteresis.

Figure 3.14: The TLV7011 picture taken from [28].

The following reasons led to its choice:

- Long lasting battery and ideal for portable application thanks to its wide operating voltage range, low quiescent current, and small package size.

- Better resistance to noise than a simple comparator: the addition of hysteresis avoids false comparator switching due to noise.

Schematically, the circuit looks as follows (figure 3.15, taken from [26]):

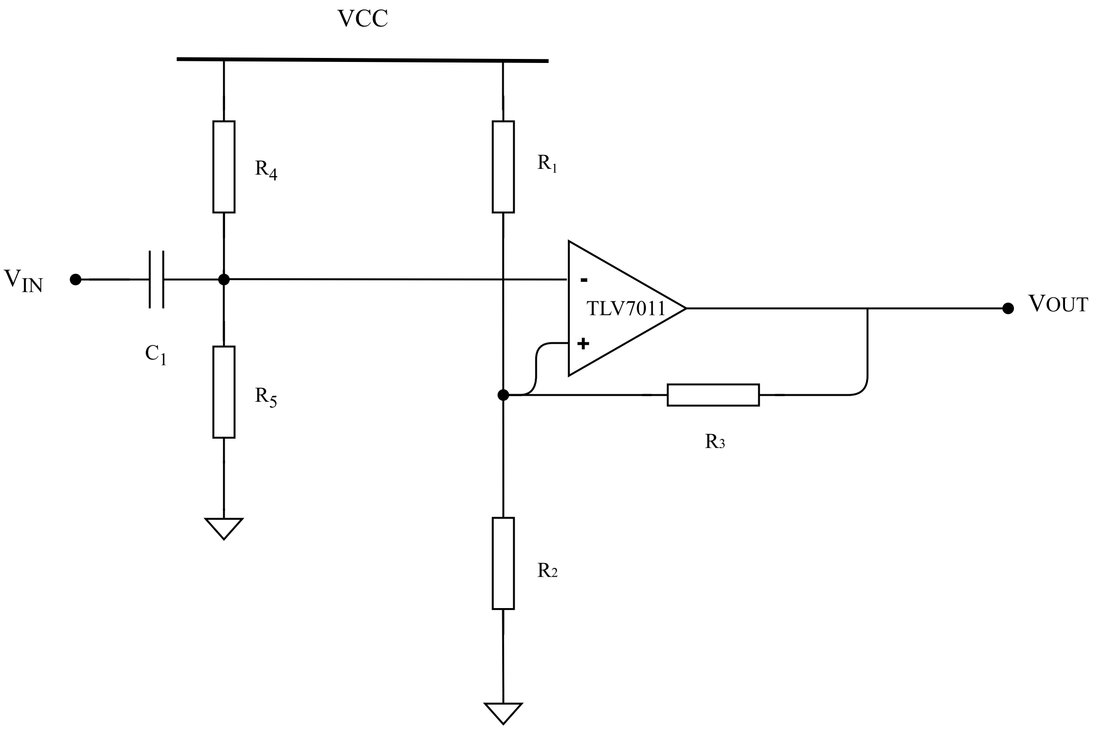

Figure 3.15: Schematic circuit of the threshold comparator. The picture is from [26].

In fig.3.15 $R_{1,2,3}$ are the three-resistor network that makes up the threshold comparator, and C_1, R_4, and R_5 are introduced to get a passive high-passing filter and to set the bias point at half the output dynamics. Moreover, this filter returns the signal to a voltage reference since TX and RX systems are separate.

First of all, as stated in [26], two bypass capacitances, with the value of 1 μF and 0.1 μF respectively, are required to decouple the threshold comparator from the power supply. Figure 3.16 depicts the bypass capacitances placed between V_{CC} and ground.
Subsequently, an analysis of what values to assign to $R_{1,2,3}$ and C_1, R_4, and R_5 is conducted.

C_1, R_4, and R_5 sizing

The main function of these components is to remove environmental noise, especially noise at 50 Hz and its first harmonics. Thus, a cut-off frequency of 10 kHz was chosen.

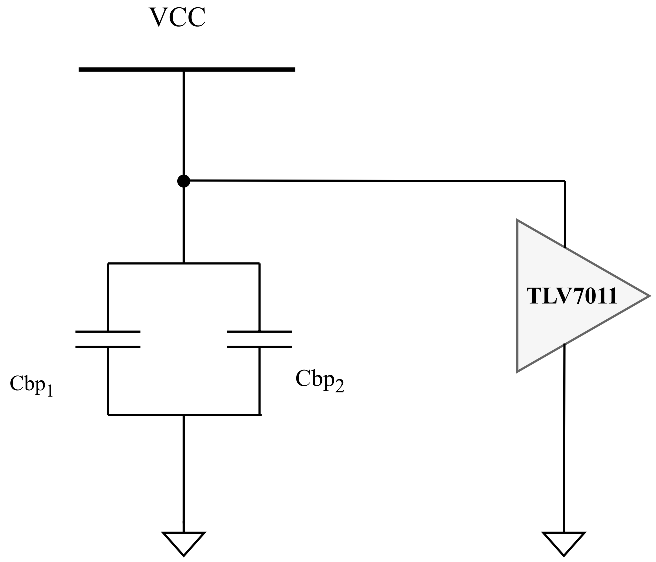

Figure 3.16: Supply voltage of the threshold comparator and by-pass capacitances [26].

Since the two resistances must have the same value to set the bias point at half the output dynamics, the calculation of $f_{cut-off}$ results from the equation 3.2:

$$f_{cut-off} = \frac{1}{2\pi(R_4||R_5)C_1} \tag{3.2}$$

By taking $C_1 = 1\,\text{nF}$, with $f_{cut-off} \simeq 10\,\text{kHz}$ the two resistances are set to $R_4 = R_5 = 33\,\text{k}\Omega$.

R_1, R_2, and R_3 sizing

As pointed out in its datasheet, the levels of the thresholds that allow the comparator to switch are determined by the equations 3.3 and 3.4, and depend on the value of the resistors R_1, R_2, and R_3.

$$V_H = V_{cc} \cdot \frac{R_2}{(R_1||R_3) + R_2} \tag{3.3}$$

$$V_L = V_{cc} \cdot \frac{R_2||R_3}{R_1 + (R_2||R_3)} \tag{3.4}$$

The difference between the two switching thresholds is called hysteresis amplitude,

ΔV = V_H - V_L.
Before explaining how the resistance values were obtained, a clarification must be made. As anticipated in subsection 3.2.1, the digital potentiometer was used as the feedback resistor of the inverting comparator with hysteresis, so R3 includes the AD5272.

The output of the comparator switches if the input signal V_{IN} (at the inverting input) transits above V_H on the way up and below V_L on the way down. The output will be a digital signal of 0 or V_{CC} value. Thus, in order for the comparator to work correctly, the values of the signal collected by the RX electrode (V_{IN} in fig.3.15) were investigated. The tests were conducted in the same way reported on pag.24, and data were taken once a day at mid-day throughout the month of June. The graph 3.17 shows the values of the peak-to-peak amplitude collected in relation to the number of measurements taken, where the first measurement was on June 7^{th}, and the last was on June 31^{st}; WE in green stands for water event. As can be seen, the amplitude values, in relation to hydration states, are maintained between 200 mV and 500 mV (range in purple in fig.3.17).
Considering the fact that electrical parameters vary according to environmental conditions, season, etc., it was chosen to take 100 mV and 600 mV as acceptable limits of hysteresis. Preliminary calculations revealed that achieving these limits with only the AD5272 as the feedback resistor would have been impossible. Because switching to a digital potentiometer with a higher full-scale resistance was not an option since it was not available in the DET laboratory's stock, the solution was found by adding a series resistor R_s. Figure 3.18 depicts the new schematic circuit of the threshold comparator.

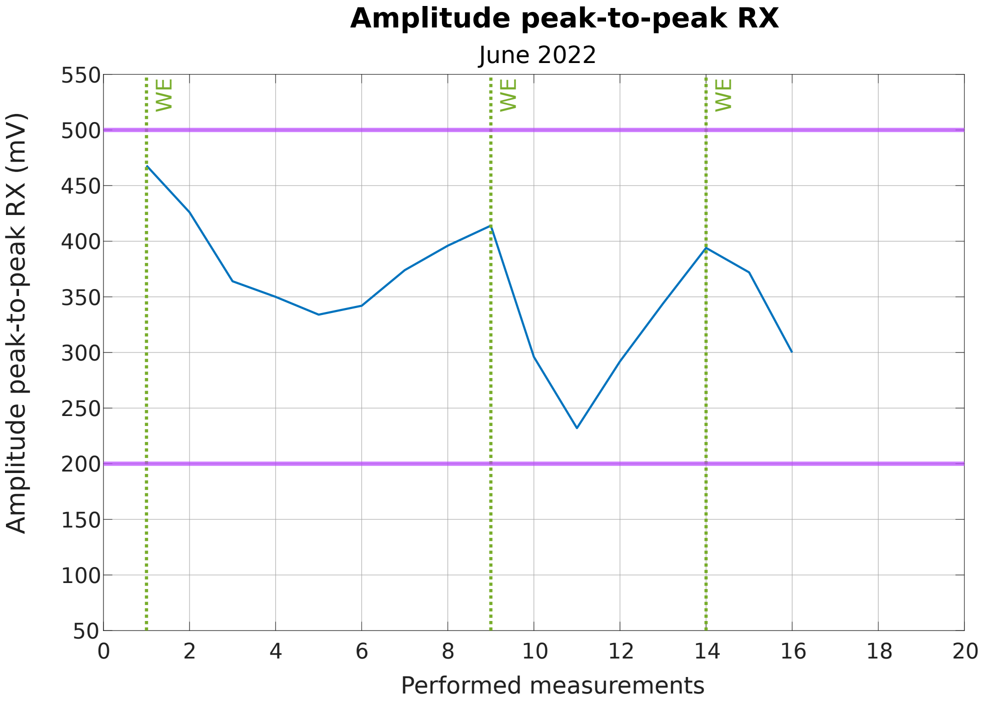

Figure 3.17: Peak-to-peak amplitude collected at the RX electrode by oscilloscope Fluke ScopeMeter 190-204 throughout June. WE stands for water event and the two lines in purple indicate the the maximum and minimum value of the amplitude found.

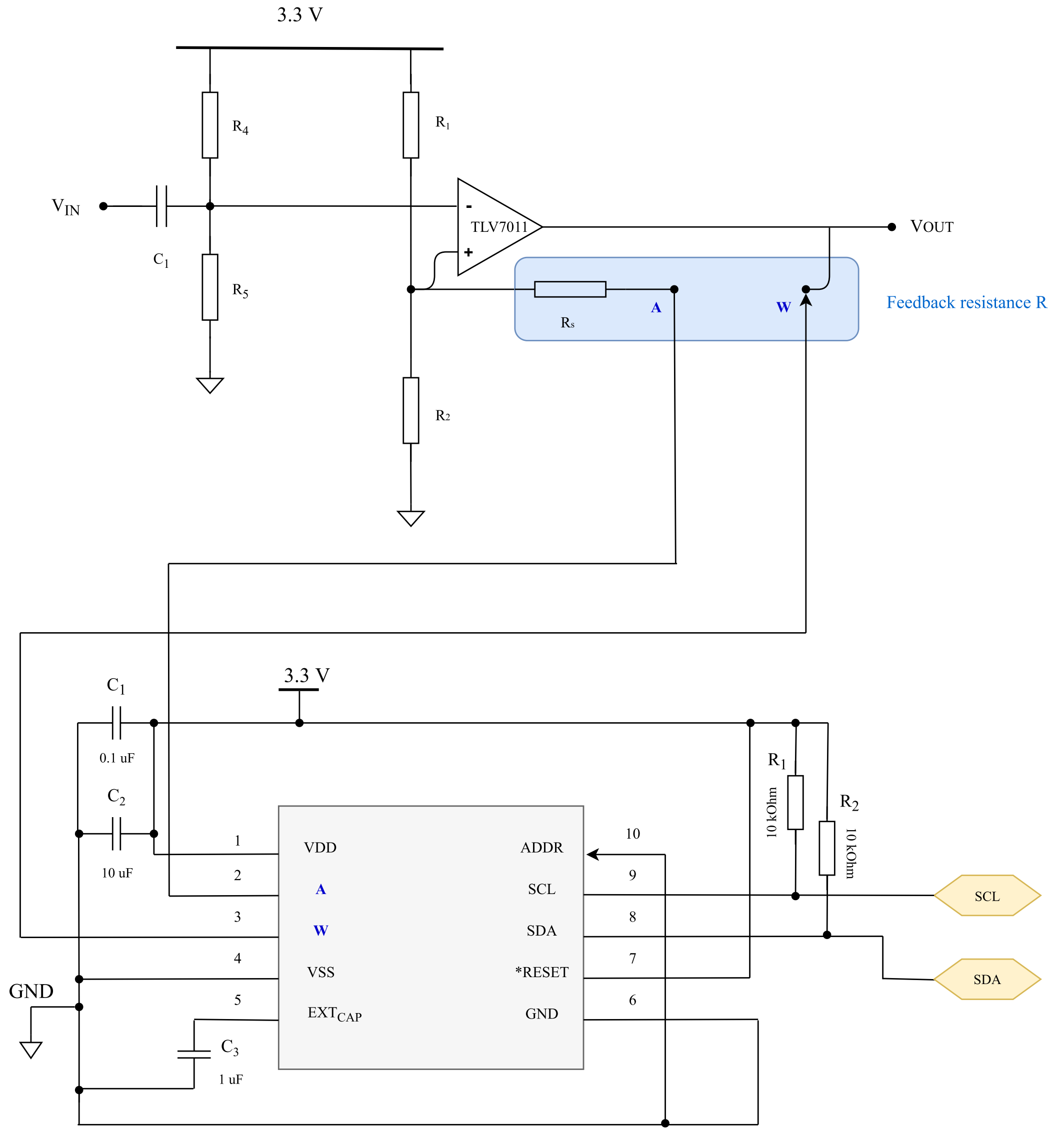

Figure 3.18: The new schematic circuit of the threshold comparator. The feedback resistor is the series between R_s and the resistance R_{WA} between pin W and A of the AD5272.

Using MATLAB, commercial resistance values for R_1, R_2, and R_s, which would allow the hysteresis limits described above to be reached, were investigated. Considering the fact that:

- R_1 and R_2 must have sufficiently high values (from the order of $k\Omega$ onwards) to decrease bias point consumption and must also be equal to make the two thresholds (V_H and V_L) symmetrical to half of the comparator's dynamics;

- to solve the equations 3.3 and 3.4, R_s and $R_{1,2}$ must be of the same order of magnitude;

the resistance values analyzed ranged from $1\,k\Omega$ to $100\,k\Omega$ for $R_{1,2}$ and from $1\,k\Omega$ up to $47\,k\Omega$ for R_s. Thus, the values of resistances that satisfy all the requirements are $R_1 = R_2 = 3.3\,\mathrm{k}\Omega$ and $R_s = 7.5\,\mathrm{k}\Omega$. The following is a table with all the components used to operate the inverting comparator properly.

Table 3.3: Components utilized in the inverting comparator.

Component	**Value**	**Type/Tolerance**
C_1	1 nF	Ceramic
R_4	33 kΩ	±1%
R_5	33 kΩ	±1%
R_1	3.3 kΩ	±1%
R_2	3.3 kΩ	±1%
R_s	7.5 kΩ	±1%
AD5272	R_{nom} = 50 kΩ	Digital Potentiometer, ±1%

Furthermore, figures 3.19 and 3.20 show the change in thresholds (V_H and V_L) and hysteresis as a function of R_3, respectively. Specifically, the potentiometer was assumed to move in steps of $48.82\,\Omega$ (D = 1 in the formula 3.1).

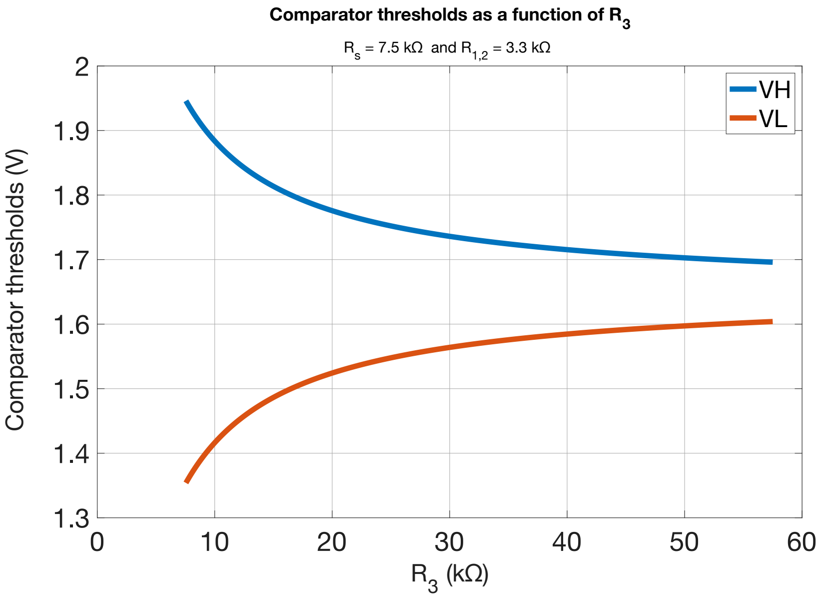

Figure 3.19: V_H and V_L as a function of R_3.

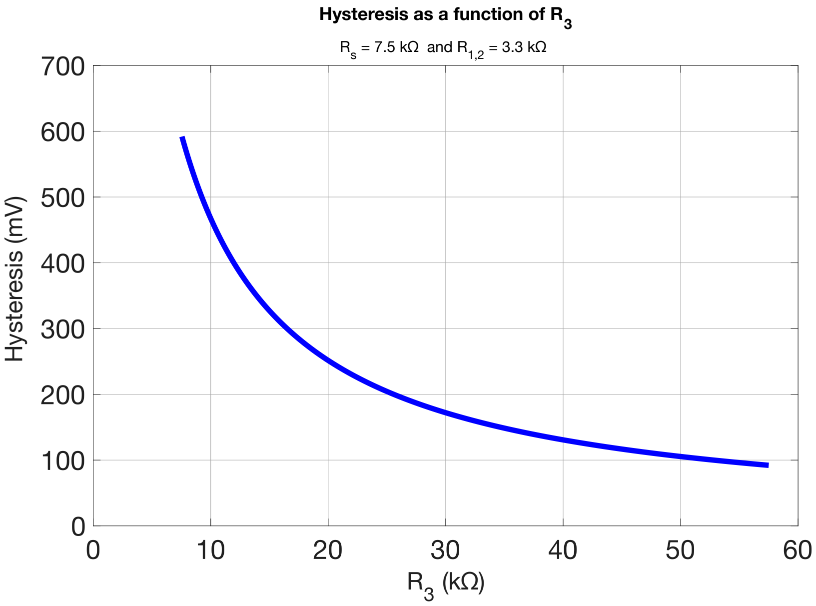

Figure 3.20: Hysteresis as a function of R_3.

AD5272 number of steps

As can be seen from fig.3.20, the constant resistance variation of the potentiometer, with fixed values of all other components, produces a nonlinear hysteresis change. As a result, the sizing of the steps was picked to have hysteresis variation always constant; 20 mV for each step was found to be the right trade-off. This choice led to the selection of 25 variations of the wiper.

In figure 3.21, the orange dots represent the potentiometer resistance (R_{pot})-Hysteresis duo that meets the requirement; also note how the change in ΔR_{pot} is not constant.

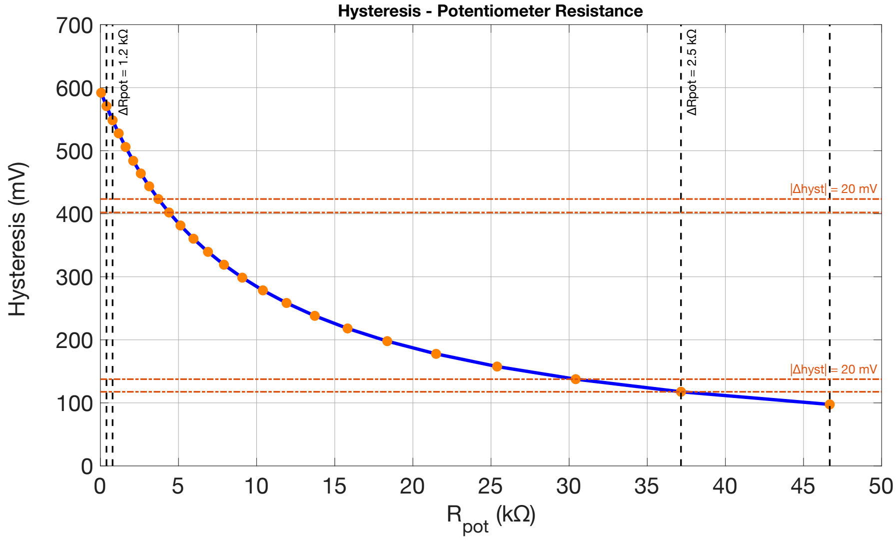

Figure 3.21: Hysteresis as resistance potentiometer R_{pot} function. The change in R_{pot} is set to result in a hysteresis variation of 20 mV.

3.2.2 Microcontroller unit

The main function of the microcontroller unit (MCU) is to communicate with the potentiometer via I^2C protocol and estimate the amplitude via a C routine.

As anticipated in the introduction of section 3.2, the microcontroller unit consists of ARM Cortex-M4 with Floating Point Unit (FPU) 32-bit RISC (Reduced Instruction Set Computer) processor mounted on a Nucleo Development Board STM32F401RE and produced by STMicroelectronics; an STM32 Nucleo board top view is shown in figure 3.22 (picture taken from UM1724 user manual).

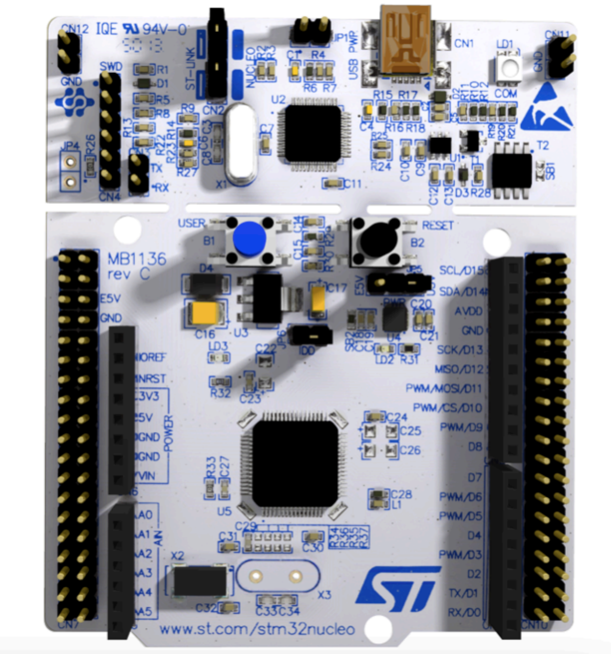

Figure 3.22: STM32 Nucleo board top view from UM1724 user manual.

It has a range of power supply $\in [1.7\ 3.6]$ V, and it supports a maximum CPU frequency of 84 MHz with a flash and RAM memory up to 512 kB and 96 kB respectively. The host PC provides the power supply through the USB cable in this application. Figure 3.23 depicts Arduino Uno V3 connectors (CN5, CN6, CN8, CN9) and ST morpho connector (CN7 and CN10) of Nucleo-F401RE. In particular, there are three ports (A, B, and C) with 16 pins each.

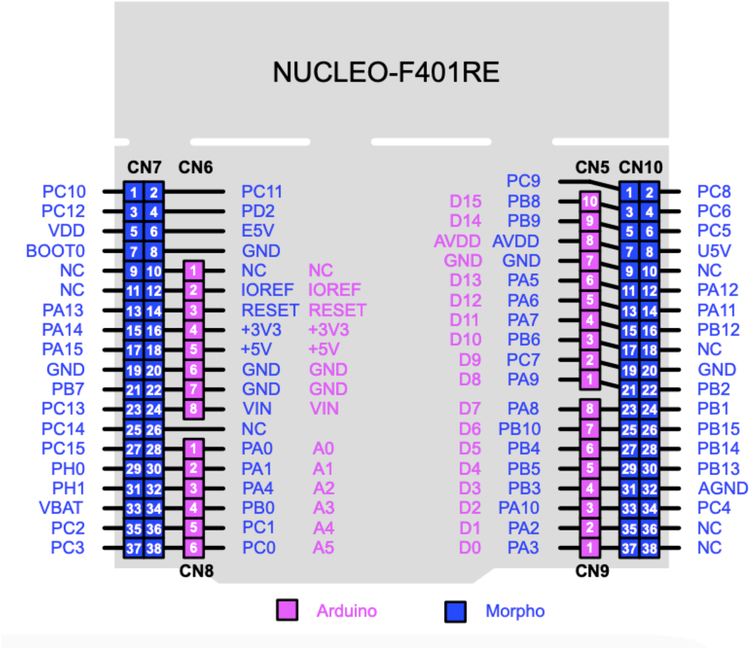

Figure 3.23: F401RE pin (picture is taken from UM1724 user manual).

Moreover, to achieve the best compromise between low power consumption, quick startup, and available wakeup sources, the device supports three low-power modes:

- **Sleep mode**: ARM Cortex-M4 core is stopped while peripherals keep running.
- **Stop mode**: it achieves the lowest power consumption while retaining the contents of SRAM and registers. Specifically, all clocks in the 1.2 V domain are stopped.
- **Standby mode**: the entire 1.2 V domain is powered off by turning off the internal voltage regulator.

The MCU is awakened by one of these modes depending on the entering mode. For example, it can be awakened by any interrupt or wakeup event in the case of sleep mode or by any external interrupt/event controller (EXTI) line in the case of stop mode. In this thesis work, the stop mode with awakening from the EXTI line was implemented, leading the system to wake up when a rising edge on that pin is detected; this decision was made because TX and RX are separate, and the receiver does not know when the signal to be analyzed arrives. Consequently, it wakes up when the inverting threshold comparator switch arrives, representing the arrival of a new measurement. Moreover, tests have shown that the plant's condition does not change significantly from hour to hour, allowing for fewer measurements to be taken daily.

With the stop mode, it is possible to achieve maximum wakeup timing of 33 μs and current consumption of $42\,\mu A/MHz$ (the values were taken from the STM32F401xE datasheet considering the voltage regulator in low power mode).

Finally, STM32CubeIDE is the advanced C/C++ development platform for managing the Nucleo board. In particular, it was employed to configure the peripheral, generate, compile and debug the code.

3.3 Complete system

After detailing the components that constitute the transmitting (section 3.1) and receiving (section 3.2) part, the schematic block diagram of the entire system architecture is shown in figure 3.24. This figure highlights the transmitting system in green and the receiving system in yellow.

It is important to underline that the output signal from the inverting comparator is sent to the MCU (as shown fig.3.24) but is driven to two different pins to do amplitude evaluation and to allow the Nucleo-F401RE to be awakened from its low power state.

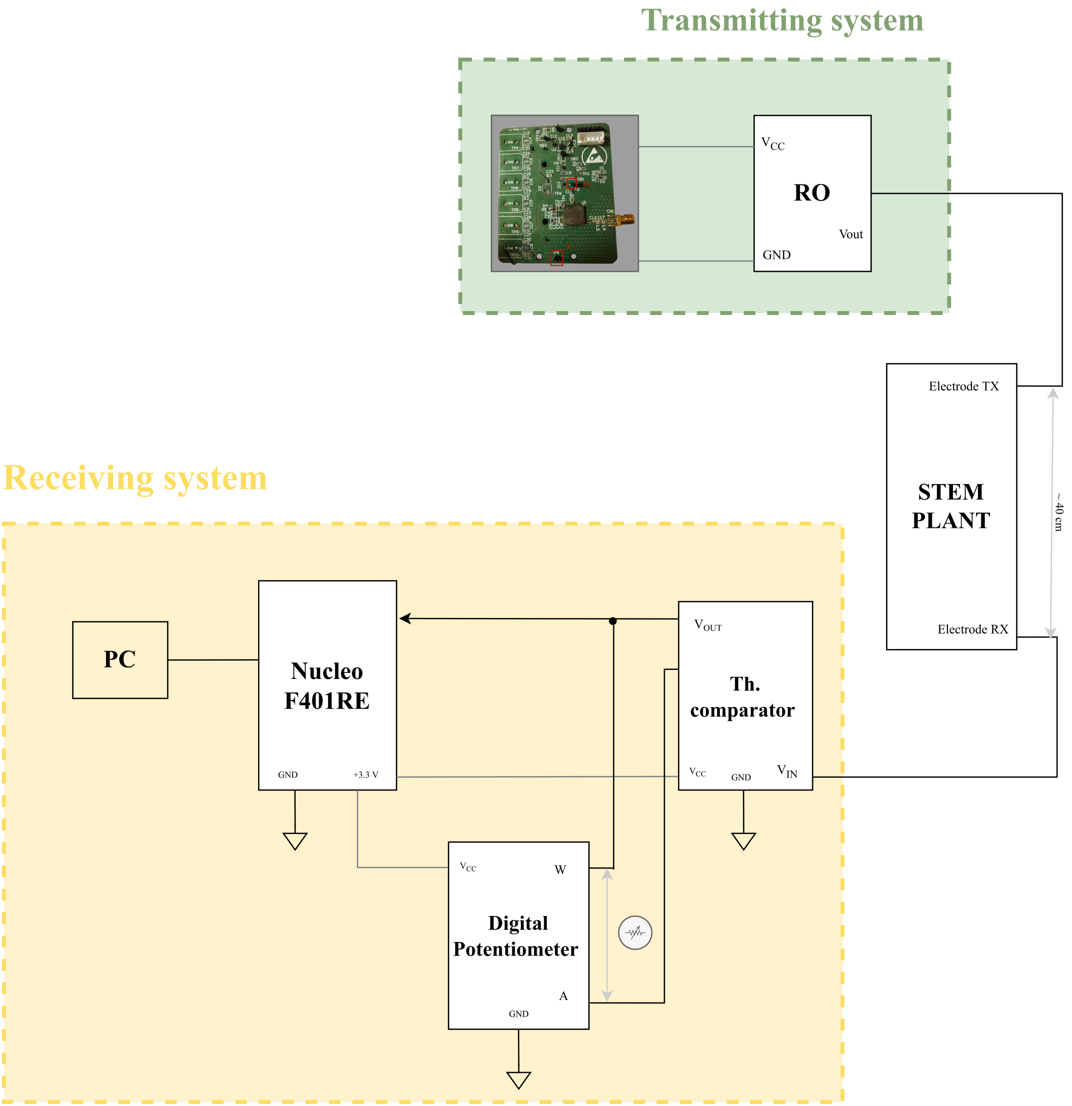

Figure 3.24: Schematic block diagram of the entire system architecture.

Chapter 4

Firmware implementation

The previous chapter described the architecture of the final system developed in this thesis work. Specifically, the injected 83.3 kHz square wave at the TX transmit electrode traveled along the stem until the electrode RX collected it. The signal at this latter electrode was sent to the input of the inverting threshold comparator for further analysis (see fig.3.24). The evaluations concentrated on analyzing its peak-to-peak amplitude to correlate a voltage measurement with changes occurring in the plant (the impedance-plant health status correlation has already been demonstrated in [15, 19]).
After deploying the hardware (chapter 3), the firmware part was implemented, programming the STM32 microcontroller, installed on Nucleo Development Board STM32F401RE, for an estimate of the RX signal's amplitude. In addition, a Python script was designed to save the amplitude values found on the PC through SPI (Serial Peripheral Interface) communication. This enabled the data to be gathered and analyzed, as described in ch.5.

This chapter is divided as follows: section 4.1 better illustrates the connection of hardware components with the Nucleo-F401RE and reports the flow chart followed for writing the C code on STM32CubeIDE; section 4.2 describes the application code, and finally, section 4.3 deals with explaining how the Python code was implemented to save the data.

4.1 Introduction

To understand the connections and the configurations of the MCU deployed, fig.3.23 and other important points from chapter 3 are recalled:

1. The MCU is responsible for powering the digital potentiometer AD5272 and the inverting comparator with hysteresis, of which TLV7011 is the operational

amplifier. For this reason, the **+3V3** and **GND** pins of the CN6 Arduino Uno V3 connector were linked to AD5272 and inverting the comparator's power supplies.

2. The MCU communicates with the AD5272 via I^2C to change the potentiometer resistance value. Since the MCU acts as the master in this communication and the potentiometer is the slave, the data must be transmitted thanks to the SDA and SCL lines (as explained in 3.2.1). Therefore, the two components' respective lines (SDA and SCL) must be connected. Pins **PB8** and **PB9** of the CN5 Arduino Uno V3 connector are the ones that have been connected with the SCL and SDA lines of the potentiometer. Moreover, to make it easier for the user to understand when the connection between AD5272 and MCU occurs, pin **PA5**, corresponding to the green LED on the Nucleo board, has been used.
3. The output signal from the inverting comparator must be sent to two different pins of the Nucleo-F401RE for two different reasons:

   (a) To wake up the MCU from the low-power state. Thus, an EXTI line corresponding to pin **PB2** of the CN10 ST morpho connector is connected with the comparator's output, leading the system to wake up when a rising edge on that pin is detected. Since TX and RX are separate systems, the MCU awakening indicates the arrival of a new amplitude measurement.

   (b) To evaluate the amplitude of the signal. To do this, as will be further explained in subsection 4.2.3, it is important to evaluate the frequency of the inverting comparator's output, which is also connected to pin **PA0** of the CN8 Arduino Uno V3 connector.

In table 4.1 a summary of the Nucleo-F401RE pins used is present.

Table 4.1: Summary of Nucleo-F401RE pins used.

Pin	**Connector**	**Function**
+3V3	CN6	V_{cc} of AD5272 and Th.comparator
GND	CN6	Ground of AD5272 and Th.comparator
PB8	CN5	SCL line (AD5272)
PB9	CN5	SDA line (AD5272)
PA5		Green LED
PB2	CN10	EXTI line
PA0	CN8	Input capture line

Figure 4.1 shows the board programming flowchart. It is divided into:

- **Orange block**: timers and peripherals are initialized. Also, since the Nucleo board is always connected to the PC in this application, it is initially set up in stop mode to decrease power consumption.

- **Green block**: this second block is responsible for managing the awakening of the MCU, and it is programmed to wake up the Nucleo-F401RE when a rising edge is detected on an EXTI line, as documented in section 3.2.2. However, a check is made on the signal frequency arriving at the MCU to ensure that the rising edge is due to the signal that must be analyzed and not environmental noise. If the signal frequency is equal to the injected one in transmission with a variation of $\pm \Delta F = 25\%$, the peak-to-peak amplitude evaluation of the signal proceeds (purple block); otherwise, the MCU returns to low power. It is essential to underline that the variation of ΔF was considered to assess the non-stable injected frequency of the square wave of the TX system caused by the parasitic capacitances of breadboard mounting and the tolerance of the components used.

- **Purple block**: this block corresponds to the amplitude peak-to-peak estimation routine, which begins by setting a specific resistance to the potentiometer. As explained in section 3.2, changing the resistance of the AD5272 results in modifying the thresholds (V_H and V_L) of the inverting comparator, which switches if the input signal transits above V_H on the rising edge and below V_L on the falling edge.
  In this application, at first, the potentiometer takes a value corresponding to its full scale (about $50\,\mathrm{k\Omega}$); this causes the comparator to have narrow thresholds (see fig.3.19 when R_3 values are high). Thus, the comparator has no problems switching. As the resistance value decreases, the distance between the two thresholds increases until it becomes so large that the comparator can no longer switch (the input signal is smaller than the amplitude of thresholds V_H and V_L).
  For this reason, every time the resistance changes, it is crucial to evaluate the signal's frequency and the comparator's thresholds. If the frequency of the comparator output signal stays around $80\,\mathrm{kHz}$, it means that the comparator can switch, and its thresholds are saved in the variables $V_{H_{old}}$ and $V_{L_{old}}$. On the contrary, when a frequency equal to $0\,\mathrm{Hz}$ is measured, it indicates that the comparator has stopped its transition, and the thresholds corresponding to this potentiometer resistance value are saved in the variables V_H and V_L. Thus, the estimated peak-to-peak amplitude collected by the RX electrode is between the difference between $V_{H_{old}}$ and $V_{L_{old}}$, and the difference between V_H and V_L.

Finally, the differences in thresholds described above are transmitted to the PC, allowing them to be picked up and analyzed.

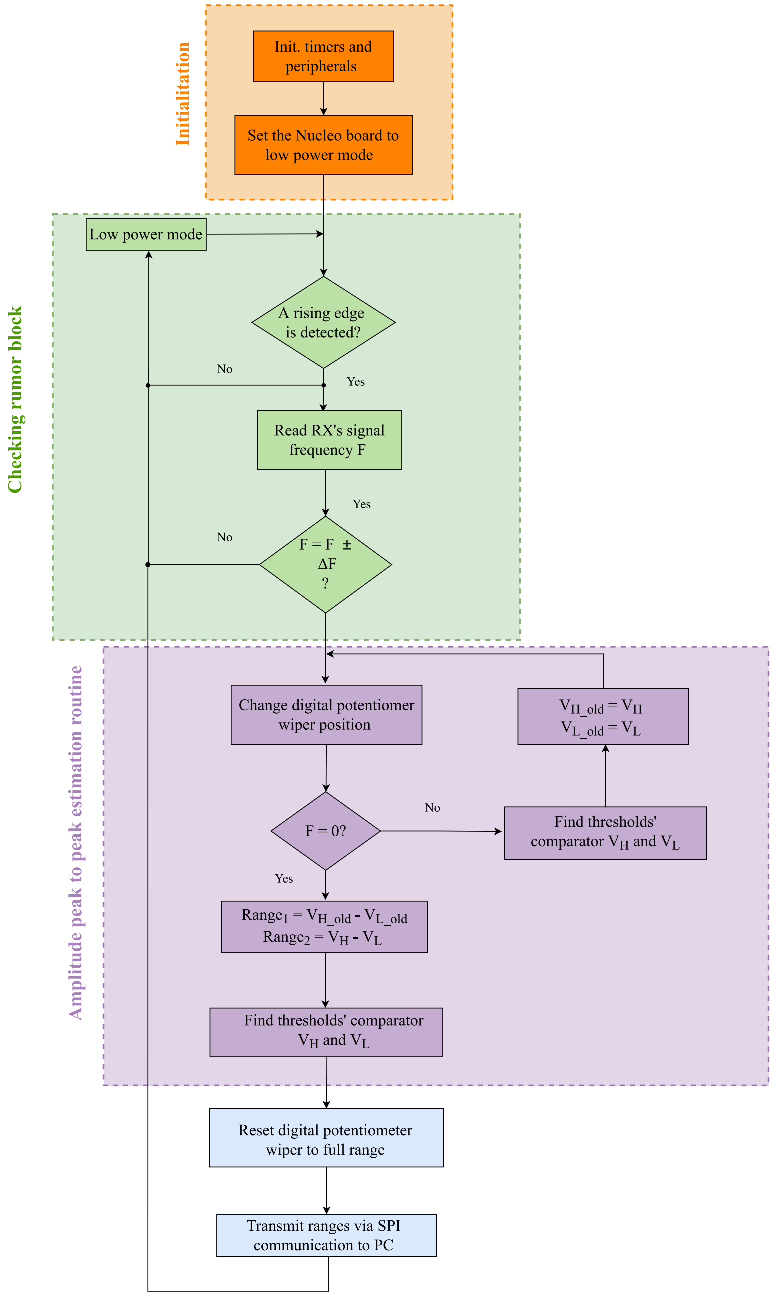

Figure 4.1: Board programming flowchart.

4.2 Application code

The software libraries used in this application are the HALs (Hardware Abstract Layers) drivers. Each driver consists of functions covering the most common peripheral features. Its development is driven by a common API standardizing the driver structure, the functions, and the parameter names. STM32CubeIDE embeds comprehensive STM32Cube MCU Packages, which include the STM32Cube HAL for the generation of configuration C code.

4.2.1 Init functions

The initialization functions are shown in listing 4.1 and are the core of the application code because they allow the peripherals to be highlighted.

Listing 4.1: Initialization code

```
1  int main(void)
2  {
3    /* MCU Configuration */
4
5    /*Reset all peripherals and Initializes the Flash interface and the
       Systick */
6    HAL_Init();
7
8    /* Configure the system clock */
9    SystemClock_Config();
10
11   /* Initialize all configured peripherals */
12   MX_GPIO_Init();
13   MX_USART2_UART_Init();
14   MX_TIM2_Init();
15   MX_TIM3_Init();
16   MX_I2C1_Init();
17 ...
18 }
```

Line 6 of listing 4.1 defines the initialization of the HAL useful for this application, as written in the introduction part of this chapter, while line 9 configures the system clock. Next, the peripherals are initialized. In particular (referring to table 4.1 for a better understanding):

- Line 12 configures the GPIO (General Purpose Input/Output) peripherals, GPIOA and GPIOB.
    - **Pin PA5** (green LED on the Nucleo board) of the GPIOA peripheral has been set to output; the status of this pin at a logic high level (LED on) defines a proper connection with the AD5272 digital potentiometer.

  Although this increases consumption, the LED was included to let the user know visually whether the system is working.
  - **pin PB2** of the GPIOB peripheral has been set to external interrupt mode with rising edge detection. In particular, when the threshold comparator switches (as explained in section 3.2), the EXTI controller's line, corresponding to the pin PB2, triggers the system to wake up by running the *EXTI line interrupt callback* (see section 4.2.2).

- Line 13 initializes the USART (Universal Asynchronous Receiver-Transmitter) peripheral. Nucleo-F401RE has three USART peripherals (1,2,6), but only UART2 has been configured in this application, allowing data transmission to the PC. An asynchronous mode and baud rate of 115,200 bit/s have been set.

- Lines 14 and 15 define the configuration of the timers' peripherals (TIM2 and TIM3). TIM2 is a 32-bit register, while TIM3 is a 16-bit one; they count up and down with the help of a programmable prescaler that divides the system's clock frequency. Moreover, they have four independent channels for input capture (IC), output compare (OC), PWM (Pulse width modulation generation), and one-pulse mode output.
  - TIM2's channel 1 (**pin PA0**) peripheral is configured in *input capture mode* with a polarity selection of rising edge and with the global interrupt enabled. Specifically, whenever a rising edge is detected on the pin PA0, the *TIM2 input capture interrupt callback* (see section 4.2.2) is fired, and the value of the timer counter register (TIMx_CNT) at that time is saved in the capture registers (TIMx_CCRx). TIM2's Channel 1 has been used to calculate the signal frequency.
  - TIM3's channel 1 peripheral is configured in *output compare no output mode* with global interrupt enabled. Channel 1 generates an interrupt (*TIM3 output compare interrupt callback* in section 4.2.2) every time a match is found between the TIMx_CCRx register (where the period to be measured must be loaded) and the counter. The application's period to count is 0.5 s.

- Line 16 initializes the I^2C peripheral. Nucleo-F401RE has three I^2C peripherals (1,2,3), but only I2C1 has been used with a 100 kHz clock speed. This enables I^2C communication with AD5272, where the NUCLEO is the master, and the digital potentiometer is the slave.

4.2.2 Interrupt callbacks

As explained in the previous subsection, the interrupt-enabled peripherals are the PB2 EXTI line, TIM3, and TIM2. Their interrupt callbacks (or ISR routines) are

reported respectively in listing 4.2, 4.3 and 4.4.
Specifically, the ISR function is called when an interrupt is fired on a specific trigger. As a result, the application program is interrupted, the program counter and the processor registers are saved in the stack, and the interrupt callback is called. The application program is resumed once the interrupt code has finished running.

EXTI line interrupt callback

When the PB2 pin detects a rising edge, the EXTI line interrupt callback starts to run. After disabling the EXTI line interrupt (line 4 in 4.2 listing), the system clock (line 5) and the SysTick (System Tick Time) are reconfigured.

Listing 4.2: EXTI line interrupt callback

```
1 void HAL_GPIO_EXTI_Callback( uint16_t GPIO_Pin) {
2
3     if(GPIO_Pin == GPIO_PIN_2){ /* A rising edge is detected on PB2 */
4         HAL_NVIC_DisableIRQ(EXTI2_IRQn); /* Disable EXTI line interrupt connected to PB2 at NVIC level */
5         SystemClock_Config(); /* Reconfigure the system clock because the main regulator was turned off */
6         HAL_ResumeTick(); /* Resume the SysTick for working with HAL DELAY */
7         low_power = 0; /* Flag that indicates low power status */
8     }
9 }
```

Once everything that had been disabled during stop mode has been resumed, the flag *low_power* (line 7), which indicates the system's state, is set to 0. In particular, it is set to 0 when the system is awake and 1 when it is in stop mode.

TIM3 output compare interrupt callback

Listing 4.3 shows the ISR called when TIM3 interrupt is fired.
TIM3 channel 1 is launched in output compare mode once the system has woken up. As stated in subsection 4.1, once the system has been awakened, it must be determined whether it was awoken by the actual signal to be analyzed or by environmental noise. For this reason, TIM3 channel 1 was chosen to count up to 0.5 s to allow the system to stabilize before checking the signal source. Thus, when a period of 0.5 s elapsed (line 4 of 4.3), the *TIM3 delay elapsed routine* is called. At line 5 of listing 4.3, flag *check*, which identifies a match of TIM3_CCR1 register and TIM3_CNT, is set to 1. Finally, TIM3 channel 1 is stopped, and the counter is reinitialized.

It should be made clear that the interrupt at the NVIC level is not enabled again until the amplitude estimation routine is complete.

Listing 4.3: TIM3 output compare interrupt callback

```c
void HAL_TIM_OC_DelayElapsedCallback(TIM_HandleTypeDef *htim)
{
    if (low_power == 0){
        if (htim->Channel == HAL_TIM_ACTIVE_CHANNEL_1){ /* TIM3 Channel 1 period elapsed */
            check=1;
            HAL_TIM_OC_Stop_IT(&htim3 , TIM_CHANNEL_1) ; /* Stop TIM3 Channel 1 */
            TIM3-> CNT=0; /* Reinitialize TIM3 counter to 0 */
        }
    }
}
```

TIM2 input capture interrupt callback

This ISR is necessary to enable frequency measurement to check the noise (green block in fig.4.1) as well as to perform the measurement routine (purple block in fig.4.1).
When PA0 (which is related to TIM2 Channel 1) detects a rising edge, an input capture interrupt is activated, and the callback depicted in listing 4.4 is triggered.

Listing 4.4: TIM2 input capture interrupt callback

```c
void HAL_TIM_IC_CaptureCallback(TIM_HandleTypeDef *htim) {
        var++; /*Variable that increases every time a rising edge is detected */
        if (var<=4){
            if ( htim->Channel == HAL_TIM_ACTIVE_CHANNEL_1){
            capture_old = capture;
            capture = TIM2 -> CNT; /* Save the capture/compare register content */
            }

        } else {
            captureDone = 1;
    }
}
```

Specifically, a counter called *var* is incremented every time this callback is called. Four fronts of the signal were measured to have a more reliable measurement of the frequency before proceeding with the frequency calculation. Thus, the values of the counter are only saved when *var* returns a value less than or equal to four.

Mainly, the first counter value, corresponding to the first rising edge, is saved in variable *capture*; when a new rising edge is detected, *capture* becomes *capture_old* and the new content of the capture/compare register, corresponding to this second edge, becomes *capture*. Once *var* is greater than four, the capture of fronts can be considered finished, and the flag *captureDone* is set to 1 to allow frequency measurements.

4.2.3 Amplitude measure routine

The routine for amplitude measure corresponds to the flowchart's purple block (fig.4.2). It is important to remember that this routine starts only after the initial check on the signal frequency (the function that measures the frequency described at the end of this subsection) has been made. Otherwise, the system returns to low power again.
Since the explanation of how this routine is performed has been explained previously (see 4.1), this part only reports the useful functions (listing 4.7, 4.5, 4.6) inside it. The programming of the digital potentiometer, which changes the feedback resistance of the inverting comparator, and the measurement of the signal's frequency are essential for calculating the range of amplitudes within which the signal will be included.

AD5272 programming

To properly program the digital potentiometer used, the following were initialized as global variables:

- address of the potentiometer with ADDR connected to ground, *pot_address*;
- number and value of steps that allow the R_{WA} resistance to change, *step_index* and *steps* respectively;

Moreover, to use the I2C HAL functions employed in this application, it was important:

- to transform the 7-bit address provided in the datasheet to an 8-bit address;
- to transmit the command (instruction to be executed, found in the datasheet) and the value to be written as a 16-bit buffer. Specifically (from most significant bits to least significant bits), the first 2 bits are irrelevant, and the next 4 bits correspond to the command (write contents of the serial register data to the control register, read contents of RDAC wiper register, etc.); the last 10 bits are the RDAC register, which contains the value of the potentiometer wiper position.

First, a check was made to see if the AD5272 was connected. If so, pin PA5 (green LED on the Nucleo board) is turned on. Secondly, RDAC register write protection

has been enabled by settling bit C1 of the control register to 1.
Listing 4.5 reports the function that allows writing to the RDAC register. It is step-dependent since the wiper assumes a different position depending on the step provided as input (steps are defined according to what is found at pag.41).

Listing 4.5: AD5272 write operation

```
1
2  uint8_t write_RDAC(int step_index){
3
4      unsigned char RDAC_buffer[2];
5      uint16_t data_send;
6      RDAC_buffer[0] = (steps[step_index] >> 8) | 0x04; /* Here to
      insert the command bites */
7      RDAC_buffer[1] = steps[step_index] & 0xFF; /* Here to insert the
      wiper position */
8      HAL_I2C_Master_Transmit(&hi2c1, pot_address, RDAC_buffer, 2, 10);
       /* Write the wiper position for changing the resistance */
9      /* Take the data sent to the RDAC register */
10     data_send = ((((uint8_t)RDAC_buffer[0] << 8) & 0xF00) |
      RDAC_buffer[1]) & (0x3FF);
11     return data_send;
12 }
```

The *RDAC_buffer* contains the write command and the resistor value to be transmitted. Line 8 of listing 4.5 reports the HAL function for transmitting this buffer. Finally, the data sent (*data_send*) is compared with the read value to the RDAC register to avoid errors.

If the value transmitted and the value read on that register are equal, the value of R_3, which is necessary for calculating the thresholds of the inverting comparator, is calculated. Listing 4.6 shows the function for the read operation.

Listing 4.6: AD5272 read operation

```
uint16_t read_RDAC(){

    unsigned char device_read[2];
    unsigned char device_check[2];
    uint16_t data_received;
    device_read[0] =0x08;
    device_read[1]= 0x00;
    HAL_I2C_Master_Transmit(&hi2c1, pot_address, device_read, 2, 10);
     /* Prepare data read from RDAC register */
    HAL_I2C_Master_Receive(&hi2c1, pot_address, device_check, 2, 10);
     /* Checking the D9–D0 value
    /* Take the data written to RDAC register to check if the value
   of the wiper is right */
```

```
    data_received = ((((uint8_t)device_check[0] << 8) & 0xF00) | device_check[1]) & (0x3FF);
    return data_received;
}
```

The *device_read* buffer contains the value 0x0800 to read the content of the RDAC wiper register; instead, *device_check* buffer includes the value of what was read. The first 6 most significant bits of this latter buffer are irrelevant, but the last 10 bits contain the value that the wiper took.

Measure frequency

Listing 4.7 reports the frequency evaluation function.

Listing 4.7: Measure frequency function

```
float measure_frequency(){
    captureDone =0;
    var =0;
    count =0; /* Variable that checks the frequency 0 */
    HAL_TIM_IC_Start_IT(&htim2, TIM_CHANNEL_1); /* Start Channel 1 of TIM2 in input capture mode, with interrupt generation */
    HAL_NVIC_EnableIRQ(TIM2_IRQn); /* Enable TIM2 interrupt at NVIC level */
    while (captureDone == 0){
        count ++;
        HAL_Delay(10);
        if (count>=15){
            captureDone = 1;
            frequency = 0;
        }

    }
        if (count<15){
            if(capture < capture_old)
                difference = capture - capture_old + 4294967295;
            else
                difference = capture - capture_old;
            frequency = (42000000/ (htim2.Instance-> PSC + 1)) / difference ; /* Evaluate the frequency */
        }
    HAL_NVIC_DisableIRQ(TIM2_IRQn); /* Disable TIM2 interrupt at NVIC level */
    HAL_TIM_IC_Stop_IT(&htim2 , TIM_CHANNEL_1) ; /* Stop TIM2 Channel 1 */
    __HAL_TIM_SET_COUNTER(&htim2, 0); /* Reset the counter */
    var = 0; /* Reset var */
    return frequency;
}
```

When this function is called, channel 1 of TIM2 is started in *input capture mode*, with interrupt generation. Since the system computes a frequency must, it must also be able to recognize when it is zero, a *count* variable has been incremented as long as the system has *captureDone* equal to 0. If the system goes into the *TIM2 input capture interrupt callback* enough times to enable the *captureDone* flag, the code exits the while and evaluates the frequency as reported on lines 17-21 of listing 4.7. Otherwise, if the system continues to have *captureDone* equal to 0 for a *count* value greater than or equal to 15, the system sets the output signal frequency at the comparator to 0. The *count* value was chosen as a good trade-off to avoid confusing the signal's oscillations with a zero frequency.
After frequency evaluation is performed, TIM2 interrupt is disabled (line 23 of listing 4.7), TIM2 channel 1 is stopped and TIM2's counter and variables are reset.

4.3 SPI communication

Once the programming phase of the board was completed, a Python script was developed to save the amplitude values transmitted by the Nucleo board. In particular, the first value transmitted corresponds to the difference between $V_{H_{old}}$ and $V_{L_{old}}$, which allowed the comparator to switch. While the second value transmitted corresponds to the difference between V_H and V_L; with these latter values, the comparator did not switch.

The flowchart 4.2 shows the program's functioning.

This code was written with the goal of saving the data in a format that would facilitate subsequent analysis in MATLAB. Firstly, the PC serial port to which the Nucleo-F401RE is connected via USB and the baud rate (equals to 115,200 bauds) are defined. Then the system waits for the data transmitted from the Nucleo board, and when it is intercepted, it is saved, along with its time and date of transmission. All received data are placed in a single file called *test.csv.* Since amplitude measurements are done manually (details will be given in chapter 5), the script is run from the command prompt whenever the data collection phase is started.

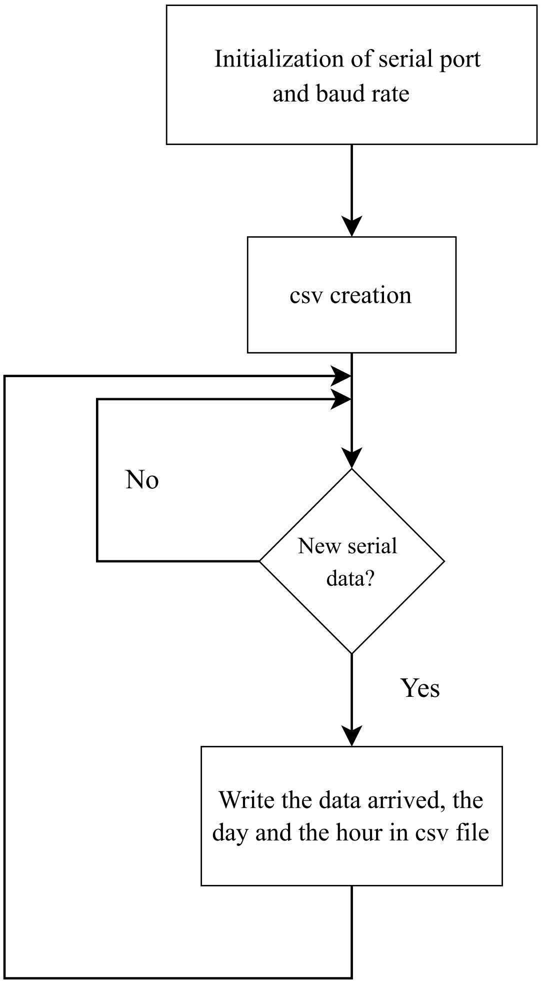

Figure 4.2: Python script flowchart for data saving.

Chapter 5

Experimental results

After the hardware and the firmware have been implemented, the analyses of the developed system on an actual plant have started. These tests were conducted on November 2022 at the DET laboratory of the Polytechnic of Turin and aimed to measure the attenuation of a signal injected in the plant steam (to review the characteristics of it, see fig.3.8), while impedance measurements are carried out.
As stated in 2.3.2 for the entire period of the thesis, the same plant and a specific stem was used to maintain consistent experimental conditions. Moreover, to assess the amplitude values of the signal that traveled within the plant stem, the components described in section 3.2 and chapter 4 were employed, manually connecting the system when the amplitude measurements were to be performed. Otherwise, the BK precision 891 impedance meter, manufactured by B&K Precision Corporation, was used to measure the impedance values (in module and phase). This analyzer uses four-terminal sensing for measurement; thus, one pair of kelvin clips was connected to the TX electrode and one to the RX electrode. Moreover, to characterize the plant under test, a frequency range between 900 Hz and 100 kHz and a phase range between $90\,^{\circ}$ and $-90\,^{\circ}$ with a logarithmic sweep mode was chosen. Figure 5.1 shows the trends of modulus and phase as a function of the inspected frequency range. These screenshots were taken from BK precision 891 during one of the stem impedance measurements.
To correlate with the tests conducted, the value of the impedance at frequency $\simeq$ 83 kHz was considered (the signal's frequency injected is 83.3 kHz, as shown in fig.3.8).

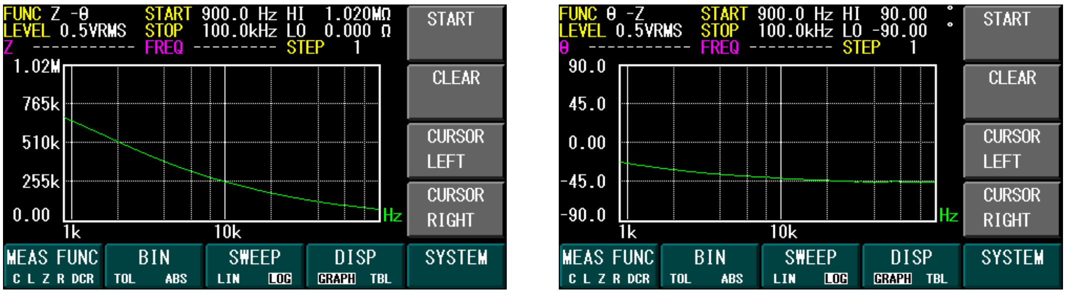

FUNC Z -θ START 900.0 Hz HI 1.020MΩ
LEVEL 0.5VRMS STOP 100.0kHz LO 0.000 Ω
Z ---------- FREQ --------- STEP 1

FUNC θ -Z START 900.0 Hz HI 90.00 °
LEVEL 0.5VRMS STOP 100.0kHz LO -90.00 °
θ ---------- FREQ --------- STEP 1

(a) (b)

Figure 5.1: Screenshots taken from BK precision 891 during one of the stem impedance measurements. Fig.5.1a and fig.5.1b show modulus and phase trends as a function of the inspected frequency range.

However, the two measurements (amplitude and phase) were not conducted simultaneously. Indeed, in a previous thesis work [26], it was discovered that the coaxial cables used in this instrument introduce a capacitance that prevents the transmitting system from properly injecting the signal into the stem [26]. Thus, plant impedance measurements have been performed by manually disconnecting the transmitter and the receiver.

Initial tests, also supported by literature [15, 19] and previous thesis work [26, 28], have shown that the variation of these electrical parameters becomes significant only after hours; as a result, few measurements were taken throughout the day from November 7^{th} to 29^{th} with two watering events, on the 8^{th} and 24^{th} evenings, respectively. The amount of water supplied was half a liter for both irrigations. The first watering event occurred after more than twenty-two days of drought, while the second occurred sixteen days after the first. Figure 5.2 compares the state of the plant on the day 7^{th} and the day 24^{th} of November before the watering event. The red circles in fig.5.2a indicate the withered leaves, while the blue rectangle frames the leaves that were starting to dry, which have subsequently been removed. Instead, in fig.5.2b, there are neither withered nor yellowed leaves.

Figure 5.3 illustrates the complete system described in the previous chapters and the instrumentation used in the actual tests. This figure highlights the transmitting design in green, the receiving system in yellow, and the instrumentation in light blue. Also, in fig.5.3, the electrodes on the plant (TX above and RX below the stem) are circled in red.

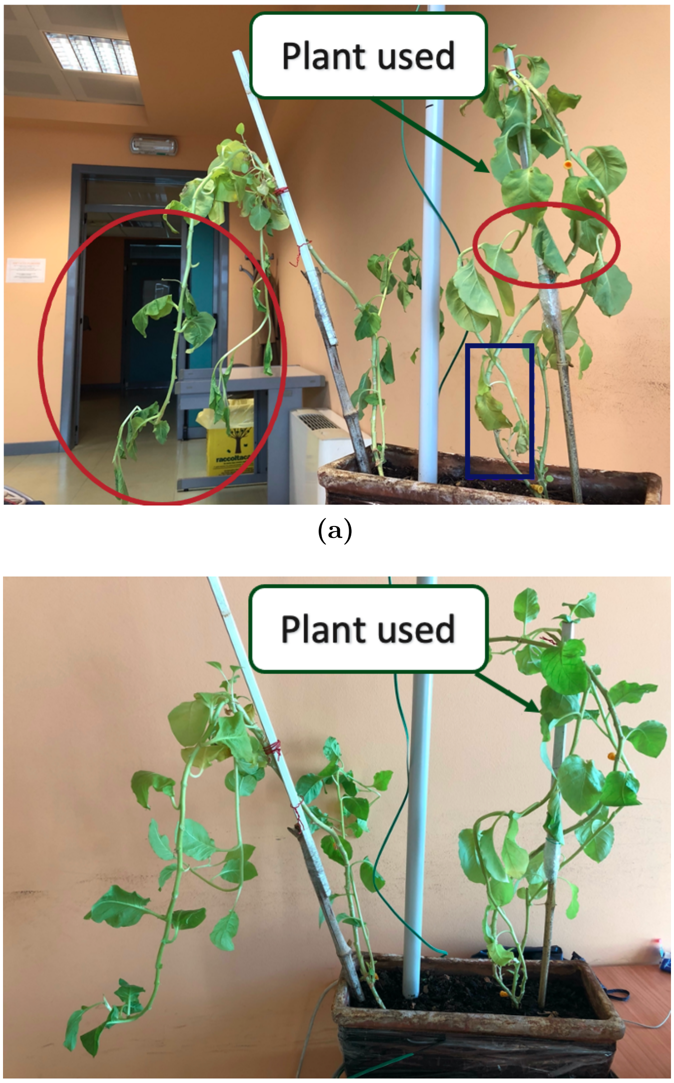

Figure 5.2: State of the plant on the day 7^{th} (fig.5.2a) and the day 24^{th} (fig.5.2b) of November. The red circles in fig.5.2a indicate the withered leaves, while the blue rectangle frames the leaves that were starting to dry, which have subsequently been removed. Instead, in fig.5.2b, there are neither withered nor yellowed leaves.

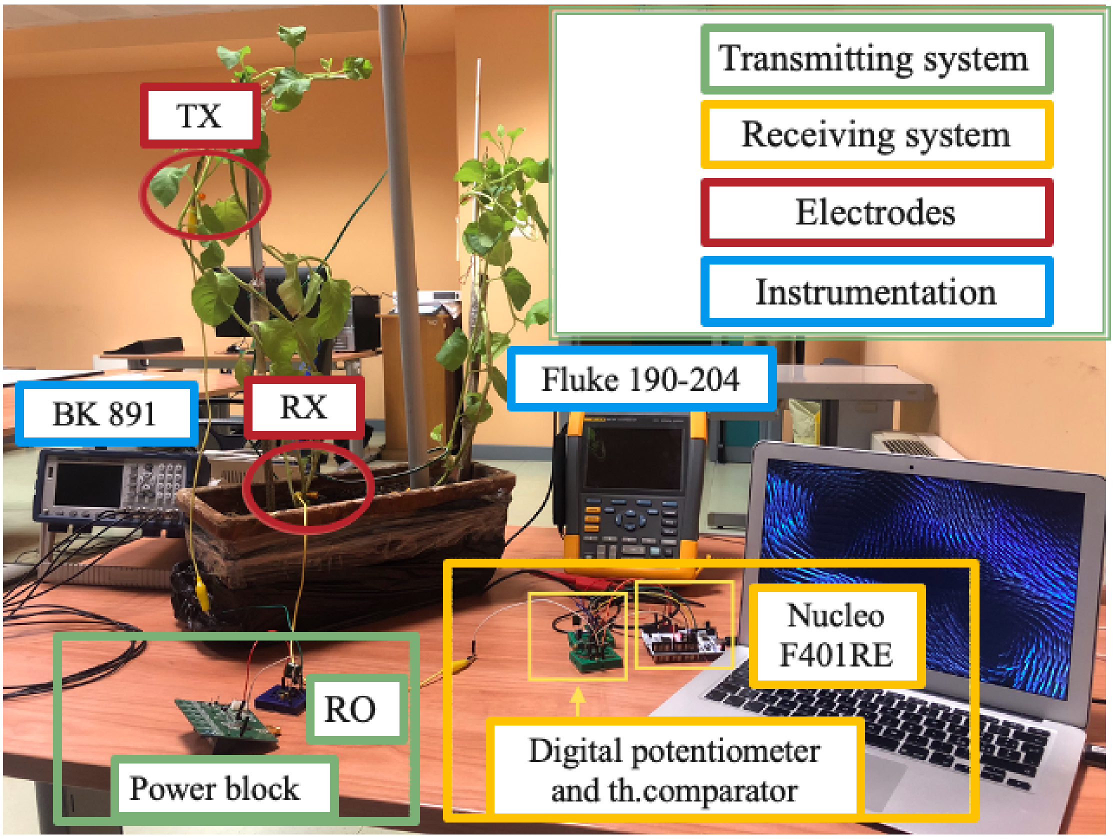

Figure 5.3: Picture of the implemented system and the instruments utilized in the laboratory experiments.

Before analyzing what was obtained from the tests, the following considerations must be made:

- Since this work is a new-born project the timed signal transmission was not included because it was decided to demonstrate a compelling correlation between signal attenuation and impedance before optimizing the system. In addition, few measurements were found to be meaningful in understanding an actual trend, as will be explained later.

- The plant to the left of the one used (fig.5.2) was not utilized for comparison because it had already been used for other purposes and showed signs of scarring where the electrodes (needles) were inserted. This suggested that the vascular system that feeds and waters those sections of the stem lacked the optimal characteristics for signal injection.
  Furthermore, multiple plant analysis was not considered because a plant with the same characteristics (soil composition, etc.) had to be used to have validity on the tests. Another plant with the same properties was not found in the laboratory, so it was chosen to focus on the life cycle of a single plant to see how it responded to signal attenuation.

- Sensors such as illumination and soil moisture were not included due to experimental conditions. The first tests using the developed device to measure RX amplitude were unsuccessful because of unexpected MHz order interference overlapping the signal. They were assumed to be caused by the air conditioner or other interference in the room, so tests were performed in another location, allowing the system to function correctly. Room-related interference issues were not considered limiting because they are assumed to be absent when the system is installed in the field.

- The graphs in this chapter will be discussed regarding the day, time, and irrigation event. Furthermore, the fact that measurements were not taken over the weekend explains the consistent trend in the graphs below.

Peak-to-peak RX amplitude

Figure 5.4 shows the amplitude trend found with the system developed in this thesis. As explained at p.48, the output of the amplitude measurement routine is transmitted as two values. In fig.5.4, the first value, in blue (*Range1*), corresponds to the first difference of the two inverting comparator thresholds found ($V_{H_{old}}$ and $V_{L_{old}}$) while the second value, in orange (*Range2*), is the second difference of the thresholds (V_H and V_L). During the early stages of testing with a portable oscilloscope, the amplitude values were checked to identify the actual value. Because the latter was always within the two differences (*Range1* and *Range2*), the peak-to-peak RX amplitude value was assumed to be the average of the two (in yellow in fig.5.4). It will be considered as the amplitude reference value for all analyses performed.

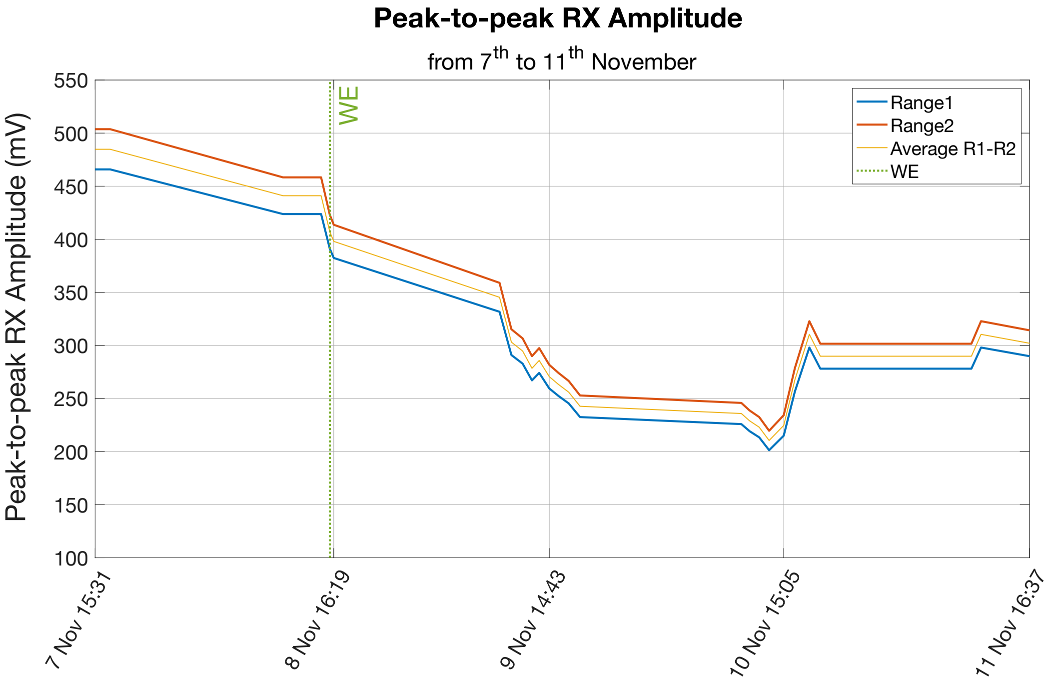

Figure 5.4: 5-day peak-to-peak amplitude trend, where *WE* stands for water event. Also, *Range1* and *Range2* are the two comparator threshold differences found, and *Average R1-R2* is the average of them.

To better focus on the explanation of the trend, the graph considers the 5-day trend from Nov. 7^{th} to 11^{th} with a water event on the 8^{th}. In November, amplitude values remained between 200 and 500 mV (as seen in the following graphs). The same amplitude range was discovered in June.

Voltage loss (fig.5.5) was also calculated, as in the formula 2.1. Throughout the tests, this value was maintained between -18 dB and -23.5 dB, leading to a percentage of attenuation of about 88% when the plant was not hydrated and 93.3% when it was. These values could be due to a partially complete knowledge of the mechanisms activated throughout the plant life cycle or the behavior of the individual plant observed. Despite this, since the same attenuations were found in both June and November, it was decided to continue the analysis with these values. Moreover, from figure 5.5, it can be seen that the two water events induced a decrease in peak voltage in RX but with a different percentage, -23 dB following the first WE and about - 21 dB following the second. An explanation will be given later based on the boundary conditions of the experiments.

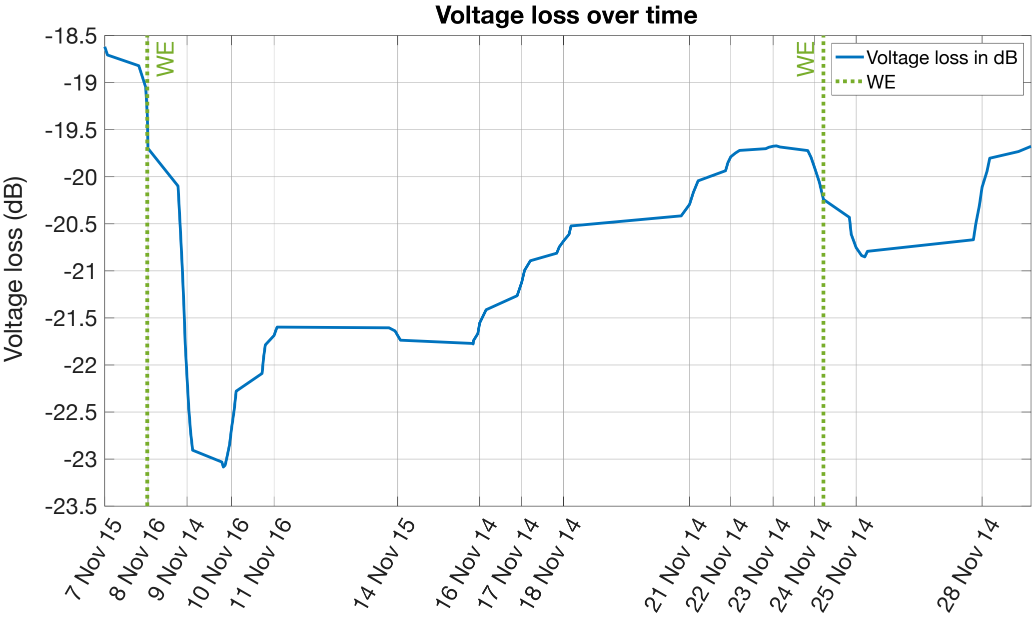

Figure 5.5: Voltage loss over time.

As seen in the literature [21], the voltage drop depends on the injection frequency. However, it also depends on the composition of the plant tissue, for example, the nature, structure, and organization of the cellular components and the amount of water they contain. Nevertheless, not all transmitted signal is expected to enter the plant's conduction channels (xylem and phloem, as section 2.3.1 reports). The electrodes are threaded inside the plant's stem, and a small signal scattering is expected at the electrodes' sides. The dispersion increases if scar tissue (due to the stem reaction to the electrode insertion or the periodic electrical stimulation [26]) forms around the electrodes. Indeed, the more necrotic the tissue becomes, the less it can transmit the signal. Figure 5.6 shows the tissue around the electrodes, whereas fig.5.6a shows one of the electrodes used in this thesis and its insertion into the stem, while fig.5.6b shows the hole formed by a previous electrode surrounded by scar tissue.

Using an electrode inserted in the stem part, as in fig.5.6b, would lead to more significant signal attenuation because of what was explained above.

(a) (b)

Figure 5.6: tissue around the insertion of the electrode. Fig.5.6a shows the tissue around one of the electrodes used in this work, while fig.5.6b shows the hole formed by a previous electrode surrounded by scar tissue.

Peak-to-peak RX amplitude and impedence

Figure 5.7 shows on the left vertical axis the amplitude values found on the days when the tests were conducted, correlated with the impedance values in modulus and phase on the right vertical axis in fig.5.7a and fig.5.7b, respectively. Boundary conditions, such as the amount of light in the environment, cause sudden fluctuations in measurements during the same day in both figures. As a result, it was decided to only label one timetable on the abscissae. Two p.m. is a good reference point for the plant to have stabilized and begun light-triggered chlorophyll photosynthesis. Furthermore, what can be observed from fig.5.7 is that the amplitude and impedance trends (both in modulus and phase) found are different depending on whether it is referred to the first watering event (WE) or the second one. In fact, before the first WE, the plant was in an overly distressed condition given by the wilted and yellowed leaves (fig.5.2a), while the second watering occurred when the plant had green and new leaves and only the soil was dry (fig.5.2b).

Next, considerations are reported by referring to the figure 5.7.

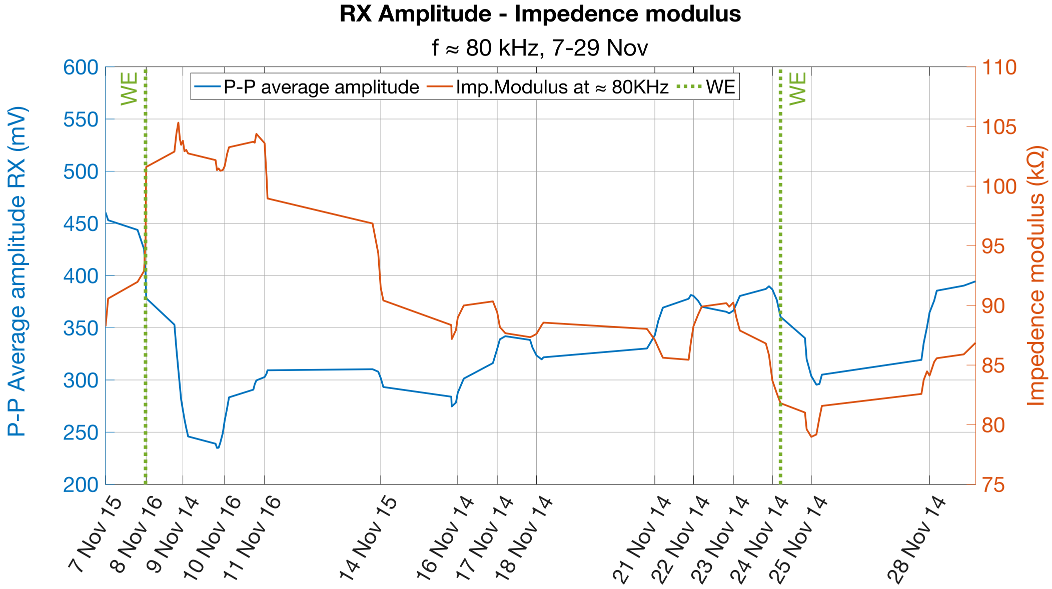

(a)

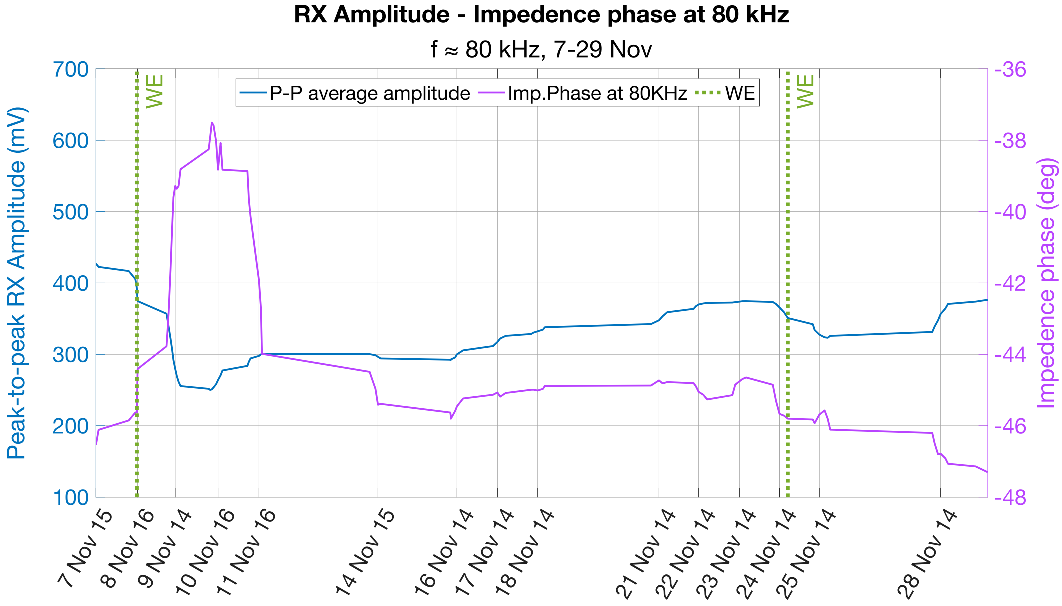

(b)

Figure 5.7: RX amplitude and impedance trends from Nov. 9^{th} to 29^{th}. Fig.5.7a reports the modulus of the impedance; instead, fig.5.7b shows the phase.

First WE - Suffering condition

Since the plant was in a distressed condition as described above and since proper irrigation of the tobacco plant should occur whenever the soil starts to be not moist, having provided the full dose of water at the same time and after more than 22 days without water is supposed to have caused an abnormal response. Indeed, it is assumed that the water supplied was excessive, causing overwatering.
Previous thesis work has shown that in the case of excessive irrigation, there is an unusual and very significant growth of the impedance module and phase, maybe caused by root asphyxiation induced by excess water in the soil [29]. The same findings can also be seen in fig.5.7a and fig.5.7b, after the first WE: both the modulus and phase of the impedance reach a maximum peak of $105\,\mathrm{k\Omega}$ and $-37.5\,\mathrm{deg}$ respectively.
Instead, the peak-to-peak RX amplitude voltage drops from $470\,\mathrm{mV}$ to $210\,\mathrm{mV}$. This latter is the lowest value observed for November, and the rapid drop is thought to be due to what was previously explained.

As the plant begins to adapt to the correct water condition, the amplitude value increases while the impedance values decrease, beginning to stabilize. On Nov.24^{th} the amplitude was about $390\,\mathrm{mV}$ and from Nov. 9^{th} to 24^{th} did not reach $470\,\mathrm{mV}$ (values found before the first WE). This trend can be explained by the fact that such high voltage values occurred when the plant was in an extreme water shortage. On day 24^{th}, the soil was moist, but it was still decided to water it to understand the trend in a normal condition of the plant's state.

Second WE - Normal condition

The second WE, as described above, occurred when the plant was in an optimal state of health (green and new leaves) with only dry soil.

The figure 5.7a shows that the amplitude follows the same trend as that observed after the first water event. It decreases until it reaches a value of $276\,\mathrm{mV}$. This value is higher than obtained after the first WE, which the plant's different conditions could explain during irrigation. In addition, it can be observed that the values take less time to rise than the nine days taken in the first irrigation. This might be because the plant did not need to stabilize but was already in an optimal condition to measure the electrical parameters.

The impedance modulus, on the other hand, decreases after irrigation, reaching a value of $78\,\mathrm{k\Omega}$. This trend is in concordance with literature [20, 19], which had discovered a direct relationship between impedance modulus decrement and

watering conditions.
Moreover, the phase pattern following the second irrigation is unusual compared to what has been found in the literature [20, 19]. Despite this, it will not be described in detail because more observations would be needed, and the amplitude-impedance correlation in modulus is optimal for drawing considerations.

Correlation

Subsequently, after analyzing the amplitude-impedance trends from a qualitative point of view, it was decided to continue the analysis quantitatively by calculating the Pearson correlation (Pearson's r) between amplitude and impedance modulus/phase (fig.5.8). Pearson's r measures the strength of the linear relationship between two variables. It has a value between -1 and 1, where -1 indicates a negative linear correlation, 0 shows no correlation, and +1 represents a positive correlation.

From fig.5.8a, it can be seen that the correlation between the peak-to-peak amplitude in RX and the impedance modulus is -0.54. It is a negative correlation that is not exactly optimal. This latter can be explained by the fact that before the two watering events, the plant was in two different conditions; as described above, the modulus trend is different following the two waterings. Thus, the different trends led to this correlation value. Indeed calculating the correlation with an equal interval between irrigations would have brought a better result.
Moreover, figure 5.8b depicts a -0.73 correlation between RX amplitude and impedance phase.

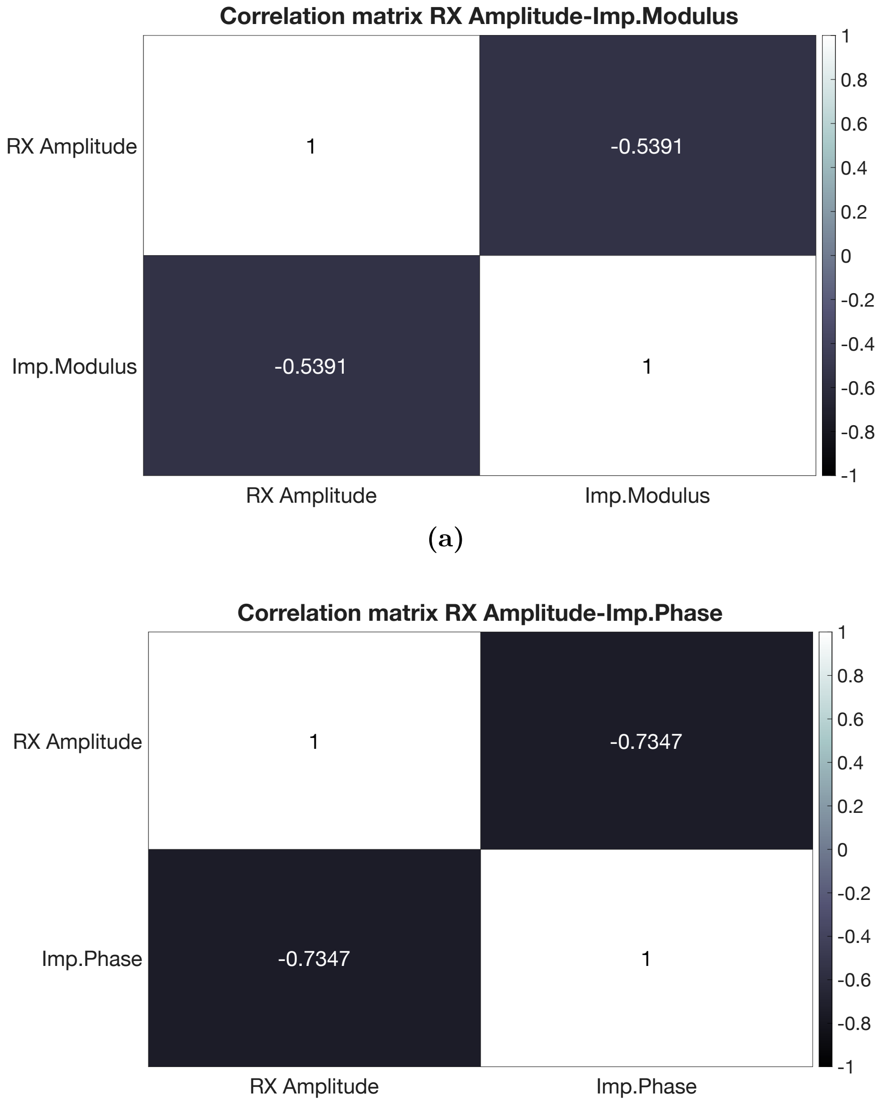

(a)

(b)

Figure 5.8: Pearson correlation. Fig.5.8a shows the correlation matrix between RX amplitude and impedance modulus; fig.5.8b depicts the correlation matrix between RX amplitude and impedance phase.

Chapter 6

Conclusion and Future perspective

This thesis presents the design of an indirect bio-impedance measurement system for plant health monitoring. The choices in developing the architecture (in transmission and receiving) and the firmware parts resulted in a system capable of estimating the signal's peak-to-peak amplitude collected at the receiving electrode with good approximation and without the aid of the ADC. The square wave injected by the transmitting electrode at a frequency of 83 kHz and its 3.6 V peak-to-peak amplitude traveled through the plant stem until it was collected at the receiving electrode. The voltage loss observed was maintained between -18 dB and -23.5 dB, leading to a percentage of attenuation between 88% and 93.3%.

Since impedance variations have been found in the literature to reveal a direct relationship with water events, the tests conducted aimed to observe a correlation between the stem's impedance at the transmitting frequency and the signal's peak-to-peak amplitude collected at the receiving electrode. This could allow the impedance, directly correlated to the plant's health, to be measured indirectly and easily.

The analyses conducted in November 2022 showed that when the impedance in modulus decreases (a sign of proper irrigation), so does the peak-to-peak amplitude collected. Since the injected wave always had the same characteristics, the decrease in stem impedance related to the decrease in amplitude of the receiving signal could be explained by the definition of Ohm's law. However, this was observed only when irrigation occurred with a non-suffering plant state. Otherwise, a positive correlation is not found. Irrigation in a condition of plant sickness leads to an opposite correlation: modulus increases while amplitude decreases. Plant-related consequences of overwatering (root asphyxiation, for example) could explain this behavior. As a result, soaking the plant in a basin of water rather than providing

water directly might not lead to a sudden increase in impedance after the irrigation since the optimal hydrated condition can be reached by the plant itself.
However, since this is the first work in this field, more testing needs to be done, especially by observing the behavior of amplitude collected and impedance modulus with regular irrigations.

The outcomes establish a foundation for indirect impedance measurement, understanding the plant's state with a simple, low-cost, and full-digital system. Indeed, with this system, two things could be measured simultaneously: plant impedance by amplitude measurement and any frequency-modulated information of the injected signal.
Moreover, since the transmission and the receiving are designed to be completely separate systems, they can be placed farther apart than 40 cm (the distance between the electrode considered in this work) and used with crops with stems longer than 1 m. Perhaps a similar system could be used to assess the health of trees. Also, since the amplitude measurement is performed without knowing when the transmission occurs, it could be thought of using the system with multiple plants to increase the scalability. For example, employing a different timing of the transmission signal for each plant would allow one receiving system to estimate the amplitude measurement of a group of plants. This would be useful in vertical farming cultivation since the number of plants per cubic meter grown is maximized, unlike in normal fields.

6.1 Possible improvements

This thesis presents a new project; consequently, many aspects still need to be improved. Below are some suggestions for improving the setup, transmit, and receive systems.

Setup

Considerations about the overall system and analyses that can be performed in future work are provided below.

- Tests done in this dissertation are preliminary. For this reason, the electronic components were mounted on breadboards and connected by jumper cables. This exposed the system to ambient noise; therefore, to avoid noise overlap, the system should be printed on two separate PCBs, one for the transmitting system and one for the receiving system.
- Tests on a larger number of plants should be conducted to determine whether the findings in this study are specific to one plant or can be generalized.
- The electrodes used are fine needles. Despite this, if left for a long time

(months or years), they lead to the formation of scar tissue on the plant, as shown in fig.5.6b, with the consequences described above. As a result, improving the electrodes could bring advancements in the plant's health and amplitude values of the signal that traveled within it. Path electrodes could be thought to be made.

- Inspecting more considerable distances between TX and RX electrodes could lead to extending health monitoring for taller stems or trees.

Transmitting system

As written in section 3.1 the transmission system in this work consists of a PCB that uses a battery to power the ring oscillator responsible for injecting the signal into the plant. The following improvements can be made:

- Change the system that powers the ring oscillator to one that does not include a battery. Using a battery involves a regular human intervention to replace or recharge them, not to mention the pollution caused by depleted batteries. Moreover, a battery's degradation and performance are critically compromised due to increased temperature. Since this system must be put into fields, it must also respond well to a change in temperature, so replacing it with other energy sources could increase the system's life. For example, supercapacitors could be used; they have a higher charge/discharge cycle and allow for better handling of current pulses (present in the case of switching to LoRA technology).
- Rather than performing amplitude measurements manually, it might be helpful to time them. Since the receiving system has already been developed to wake up and complete the amplitude measurement regardless of when the transmitting system is powered, it would be sufficient to integrate an energy-autonomous electronic transmitting system, such as the one developed in [26] to automate the procedure.

Receiving system

The way the receiver system was designed was efficient enough to estimate the peak amplitude measurement at the RX electrode. Despite this, improvements to increase performance can be made:

- Using a LoRa development kit could allow the board's USB connection with the PC to be removed and would lead to the introduction of IoT technology into this system.
- To reduce system consumption:
  - The last step of the potentiometer that allowed the measurement routine to estimate the peak amplitude of the signal that traveled through the stem could be saved. Because the values do not change significantly

throughout the day, the potentiometer does not need to perform all of the steps; it would suffice to begin one or two before the last one.

- A digital potentiometer with a larger full-scale resistance could be used. This would increase the values of the resistors that set the thresholds of the inverting comparator with hysteresis, keeping the same threshold range and decreasing the current.

Bibliography

[1] Hannah Ritchie, Max Roser, and Pablo Rosado. «CO and Greenhouse Gas Emissions». In: *Our World in Data* (2020). https://ourworldindata.org/co2-and-other-greenhouse-gas-emissions (cit. on pp. 1, 2, 4, 5).

[2] Hannah Ritchie and Max Roser. «Forests and Deforestation». In: *Our World in Data* (2021). https://ourworldindata.org/forests-and-deforestation (cit. on pp. 1, 2).

[3] Hannah Ritchie and Max Roser. «Environmental Impacts of Food Production». In: *Our World in Data* (2020). https://ourworldindata.org/environmental-impacts-of-food (cit. on pp. 3, 4).

[4] Dániel Fróna, János Szenderák, and Mónika Harangi-Rákos. «The challenge of feeding the world». en. In: *Sustainability* 11.20 (Oct. 2019), p. 5816 (cit. on pp. 4, 5).

[5] *Consequences of climate change.* `https://climate.ec.europa.eu/climate-change/consequences-climate-change_en` (cit. on p. 4).

[6] David R Williams, Michael Clark, Graeme M Buchanan, G Francesco Ficetola, Carlo Rondinini, and David Tilman. «Proactive conservation to prevent habitat losses to agricultural expansion». en. In: *Nat. Sustain.* 4.4 (Apr. 2021), pp. 314–322 (cit. on p. 5).

[7] `https://www.maplecroft.com/` (cit. on p. 5).

[8] Achim Walter, Robert Finger, Robert Huber, and Nina Buchmann. «Opinion: Smart farming is key to developing sustainable agriculture». en. In: *Proc. Natl. Acad. Sci. U. S. A.* 114.24 (June 2017), pp. 6148–6150 (cit. on p. 6).

[9] Bam Bahadur Sinha and R Dhanalakshmi. «Recent advancements and challenges of Internet of Things in smart agriculture: A survey». en. In: *Future Gener. Comput. Syst.* 126 (Jan. 2022), pp. 169–184 (cit. on p. 6).

[10] Jehangir Arshad, Musharraf Aziz, Asma A Al-Huqail, Muhammad Hussnain uz Zaman, Muhammad Husnain, Ateeq Ur Rehman, and Muhammad Shafiq. «Implementation of a LoRaWAN based smart agriculture Decision Support System for optimum crop yield». en. In: *Sustainability* 14.2 (Jan. 2022), p. 827 (cit. on p. 6).

[11] V. Palazzi, F. Gelati, U. Vaglioni, F. Alimenti, P. Mezzanotte, and L. Roselli. «Leaf-Compatible Autonomous RFID-Based Wireless Temperature Sensors for Precision Agriculture». In: *2019 IEEE Topical Conference on Wireless Sensors and Sensor Networks (WiSNet)*. 2019, pp. 1–4. DOI: `10.1109/WISNET.2019.8711808` (cit. on pp. 6, 7).

[12] K A Patil and N R Kale. «A model for smart agriculture using IoT». In: *2016 International Conference on Global Trends in Signal Processing, Information Computing and Communication (ICGTSPICC)*. Jalgaon, India: IEEE, Dec. 2016 (cit. on p. 6).

[13] Pradeep Kumar Singh and Amit Sharma. «An intelligent WSN-UAV-based IoT framework for precision agriculture application». en. In: *Comput. Electr. Eng.* 100.107912 (May 2022), p. 107912 (cit. on p. 6).

[14] Cheng Zhang, Yanyou Wu, Yue Su, Deke Xing, Yi Dai, Yansheng Wu, and Lei Fang. «A plant's electrical parameters indicate its physiological state: A study of intracellular water metabolism». In: *Plants* 9 (10 Oct. 2020), pp. 1–16. ISSN: 22237747. DOI: `10.3390/plants9101256` (cit. on p. 7).

[15] Umberto Garlando, Lee Bar-On, Paolo Motto Ros, Alessandro Sanginario, Sebastian Peradotto, Yosi Shacham-Diamand, Adi Avni, Maurizio Martina, and Danilo Demarchi. «Towards optimal green plant irrigation: Watering and body electrical impedance». In: *2020 IEEE International Symposium on Circuits and Systems (ISCAS)*. Seville, Spain: IEEE, Oct. 2020 (cit. on pp. 7, 10, 16, 17, 19, 24, 46, 61).

[16] Rachnarin Nitisoravut and Roshan Regmi. «Plant microbial fuel cells: A promising biosystems engineering». en. In: *Renew. Sustain. Energy Rev.* 76 (Sept. 2017), pp. 81–89 (cit. on p. 7).

[17] Edith Osorio de la Rosa, Javier Vázquez Castillo, Mario Carmona Campos, Gliserio Romeli Barbosa Pool, Guillermo Becerra Nuñez, Alejandro Castillo Atoche, and Jaime Ortegón Aguilar. «Plant microbial fuel CellsBased energy harvester system for self-powered IoT applications». en. In: *Sensors (Basel)* 19.6 (Mar. 2019), p. 1378 (cit. on p. 8).

[18] Lee Bar-On, Umberto Garlando, Marios Sophocleous, Aakash Jog, Paolo Motto Ros, Nir Sade, Adi Avni, Yosi Shacham-Diamand, and Danilo Demarchi. «Electrical modelling of in-vivo impedance spectroscopy of Nicotiana tabacum plants». In: *Front.Electron.* 2 (Sept. 2021) (cit. on pp. 10, 19, 24).

[19] Umberto Garlando, Lee Bar-On, Paolo Motto Ros, Alessandro Sanginario, Stefano Calvo, Maurizio Martina, Adi Avni, Yosi Shacham-Diamand, and Danilo Demarchi. «Analysis of in vivo plant stem impedance variations in relation with external conditions daily cycle». In: *2021 IEEE International Symposium on Circuits and Systems (ISCAS)*. Daegu, Korea: IEEE, May 2021 (cit. on pp. 10, 18, 24, 46, 61, 69, 70).

[20] Umberto Garlando, Stefano Calvo, Mattia Barezzi, Alessandro Sanginario, Paolo Motto Ros, and Danilo Demarchi. «Ask the plants directly: Understanding plant needs using electrical impedance measurements». In: *Computers and Electronics in Agriculture* 193 (Feb. 2022). ISSN: 01681699. DOI: `10.1016/j.compag.2022.106707` (cit. on pp. 10, 24, 69, 70).

[21] Paolo Motto Ros, Enrico Macrelli, Alessandro Sanginario, Yosi Shacham-Diamand, and Danilo Demarchi. «Electronic System for Signal Transmission Inside Green Plant Body». In: *2019 IEEE International Symposium on Circuits and Systems (ISCAS)*. 2019, pp. 1–5. DOI: `10.1109/ISCAS.2019.8702577` (cit. on pp. 10, 15, 24, 66).

[22] William J Tomlinson, Stella Banou, Christopher Yu, Milica Stojanovic, and Kaushik R Chowdhury. «Comprehensive survey of galvanic coupling and alternative intra-body communication technologies». In: *IEEE Commun. Surv. Tutor.* 21.2 (2019), pp. 1145–1164 (cit. on pp. 10–12).

[23] Stella Banou, Meenupriya Swaminathan, Guillem Reus Muns, Davy Duong, Farzana Kulsoom, Pietro Savazzi, Anna Vizziello, and Kaushik R. Chowdhury. «Beamforming Galvanic Coupling Signals for IoMT Implant-to-Relay Communication». In: *IEEE Sensors Journal* 19.19 (2019), pp. 8487–8501. DOI: `10.1109/JSEN.2018.2886561` (cit. on pp. 12, 13).

[24] Aakash Jog, Lee Bar-on, Adi Avni, and Yosi Shacham-Diamand. «Feasibility of signal transmission for plant body channel communication in tobacco». In: *2020 IEEE SENSORS*. Rotterdam, Netherlands: IEEE, Oct. 2020 (cit. on p. 14).

[25] Jae Hoon Jung and Chung Mo Park. «Vascular development in plants: specification of xylem and phloem tissues». en. In: *J. Plant Biol.* 50.3 (June 2007), pp. 301–305 (cit. on pp. 18, 19).

[26] Stefano Calvo. *An energy autonomous electronic transmitting system for green plant sensing applications* (cit. on pp. 19, 22, 33–35, 61, 66, 74).

[27] Mattia Barezzi. *Long-range low-power electronic system for precision agriculture* (cit. on p. 21).

[28] Francesca Angelini. *Development of an autonomous plant monitoring system based on Plant Microbial Fuel Cells* (cit. on pp. 33, 61).

[29] Stefania Sceusa. *Studio dell'impatto dello stress idrico sull'impedenza del fusto della pianta* (cit. on p. 69).